EUROPEAN ORGANIZATION FOR NUCLEAR RESEARCH
ORGANISATION EUROPEENNE POUR LA RECHERCHE NUCLEAIRE

CERN - PS DIVISION

COMPARISON BETWEEN MEASUREMENTS AND THEORETICAL CALCULATIONS FOR A COUPLE OF AD QUADRUPOLES

G. De Ninno

Abstract

A comparison between measurements and results provided by 2D and 3D simulations performed on two families of AD quadrupoles is presented. The main aim is the theoretical estimate of the pseudo-octupolar component due to stray field in order to check the model proposed in Ref. 5, and the improvement of the calculation of the chromatic behaviour of the AC and AD tunes.

Comparison between measurements and theoretical calculations for a couple of AD quadrupoles

by:

G. De Ninno

1 Introduction

The 57 AD (AC) quadrupoles are of three different types: QN, QWS and QWSS.

The N(arrow) quadrupoles provide a pure quadrupolar field whereas the W(ide) ones are non symmetric [1] so as to generate a finite sextupolar component [2] that was designed to compensate the AC's chromaticity.

The magnetic characteristics of each family (like magnetization, homogeneity, effective length, etc.) have been measured in the past [1] for the current range suitable to the AC's operation, ($1000\,A< I < 2000\,A$).

The intent of decelerating the beam during the AD cycle down to 0.1 GeV/c requires the experimental knowledge of the same characteristics also for currents less then 1000 A and for this purpose a set of measurements [2] has been recently performed for a QN (QDN) and a QWS (QDWS7) quadrupole.

The aims of the present work are:

• A comparison between the measurements and (2D and 3D) simulations performed using the program OPERA [3,4] for two W quadrupoles;

• The theoretical estimate of the pseudo octupolar component of the end field and the check of the model proposed in [5];

• The theoretical estimate of the octupolar field generated by the two W quadrupoles;

• The attempt to improve the lattice model to obtain better agreement between the experimental chromatic behaviour of the AC's tunes and the calculated one.

---

[1]The N quadrupoles are symmetric respect to the vertical and horizontal planes and their poles show a $\pi/4$ symmetry; the W quadrupoles are symmetric only with respect to the horizontal plane. The ends of their poles are characterized by non symmetric pole shims.

[2]This sextupolar component is strong (compared with the other multipolar components generated by the quadrupole) for the WS quadrupoles and very strong for the WSS ones.

This final task has an intrinsic limitation that is common to every effort aimed to compare theoretical calculations and measurements for AC: the modelling of the lattice (based on [6]) does not seem to have the extremely high accuracy required to predict subtle chromatic effects.

In fact the parameter list [6] does not include the result of magnetic measurements performed in the 1987 [1] which are more close to the real characteristic of the machine. This means that one can only expect a general agreement between calculations and chromatic measurements.

Concerning in particular the sextupolar gradient generated by the W quadrupoles the nominal values given in [6] have to be considered as an approximation only: in fact they have been obtained by adding to the field provided by the "body" of the magnets the effects due to the end-shims and due to a particular configuration of a set of "washers" that can be moved (or removed) by the magnet expert to vary the sextupolar (and octupolar) strengths inside a certain range.

Actually the knowledge of the correspondence between the configuration of the "washers" and the values of the gradients permits one to establish the exact sextupolar (and octupolar) field generated by the W quadrupoles. This knowledge can be used to minimize the chromaticity in the AD.

2   2D analysis

A model solution with OPERA 2D [3] consists of 3 phases: data preparation (pre-processing), analysis and results display (post-processing).

The possibility to represent a quadrupol by a two dimensional model is based on the fact that it has a uniform cross-section over a length which is much larger than the gap (radius of inscribed circle) such that the field is approximated by that of an infinitely long structure. The post-processing of the data provided by the program allows to build up the magnetization curve (that is $G_0 = G_0(I)$) and the homogeneity curve (that is $(G(x) - G_0)/G_0 - (G'_0/G_0)x$) for different values of the current as well as to perform the Fourier analysis in order to estimate the higher order component of the magnetic field.

We use x,y,z for the horizontal, verical and longitudinal coordinate respectively; $G(x) = (\dfrac{\partial B_z}{\partial x})_{y=0}$ is the field gradient in the center plane (z=0) and $G_0 = G(x = 0)$.

2.1   QD7: comparison between 2D model and measurements

Fig. (1) shows the experimental and the theoretical magnetization curve for QD7 [3].

The comparison indicates that the model overestimates the saturation effect (that is the deviation of $G_0(I)$ from a linear behaviour). To explain this fact we have to consider in more detail the modeling of a laminated magnet (as is the case of the AD's quadrupoles). A way to take into account that a part of the magnetic flux passes through the isolating sheets is to reduce

---

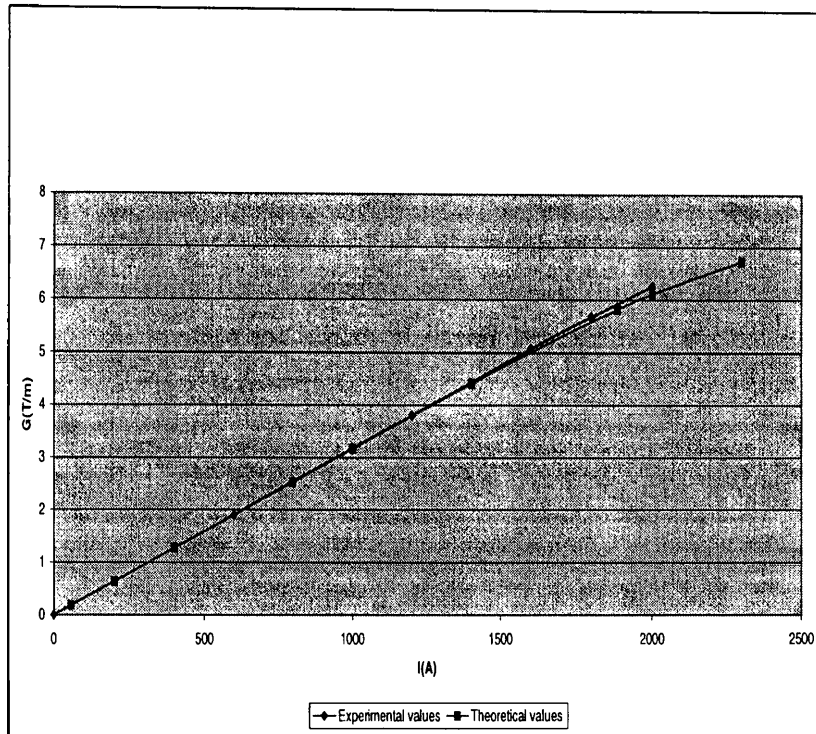[3]The 2D and 3D model for QDW7 has been developed by G. Borri.

Figure 1: Experimental and theoretical magnetization curve $G_0(I)$ for QD7. The theoretical curve is calculated assuming lamination with a stacking factor of 73%.

the effective magnetic field B by a fixed percentage. This is equivalent to a reduction of the permeability $\mu = B/H$ of the material and the lower the stacking factor, the sooner the iron reaches the saturation.

The standard percentage reduction taking only into account the ratio between iron and isolating material (about 4%) would not lead to the difference between model and measurements shown in fig. (1). A further source of saturation comes from the fact that in the two end regions of the magnet the flux lines of the field are more densely packed. This can be included in the 2D model by a further reduction of the stacking factor. For the model considered the total reduction has been fixed at 27%.

As shown in tab. 1 this allows a fair prediction of the normalized sextupolar gradient but, compared with the 4% reduction, the forseen value of the gradient (as well as the magnetization curve) is more far from measurements.

3

	Measured value	$\sigma = 27\%$	$\sigma = 4\%$
G_0 (T/m)	-6.134	-5.962	-6.151
G_0'/G_0 (m^{-1})	1.462	1.432	1.553

Table 1: QD7: Comparison between measured and calculated gradients G_0 and G_0'/G_0 at I=1948 A. The results of the calculation are for two different values of the stacking factor σ.

Figs. (2), (3) and (4) show a comparison between the measured normalized homogeneity curves and the theoretical results for different current values.
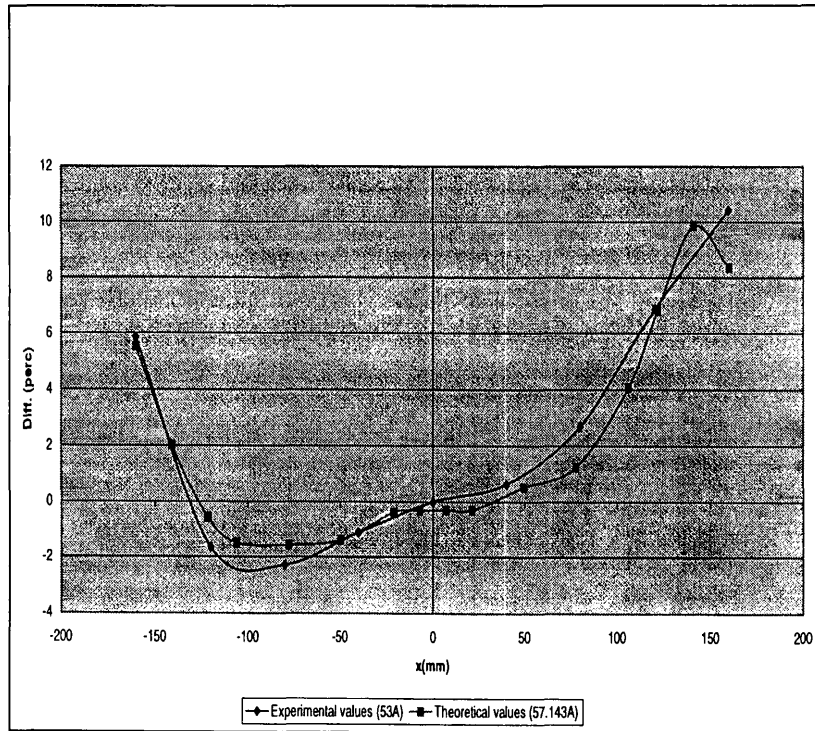
Figure 2: Experimental and theoretical homogeneity curve (I=50 A) for QD7.

The nominal value of the normalized sextupolar gradient [7] $G_0'/G_0 = 1.462$ has been chosen according to the need of compensating the AC chromaticity for a working point I=1948 A (3.5 GeV/c). For this value of the current the experimental curve is almost flat [2] and this
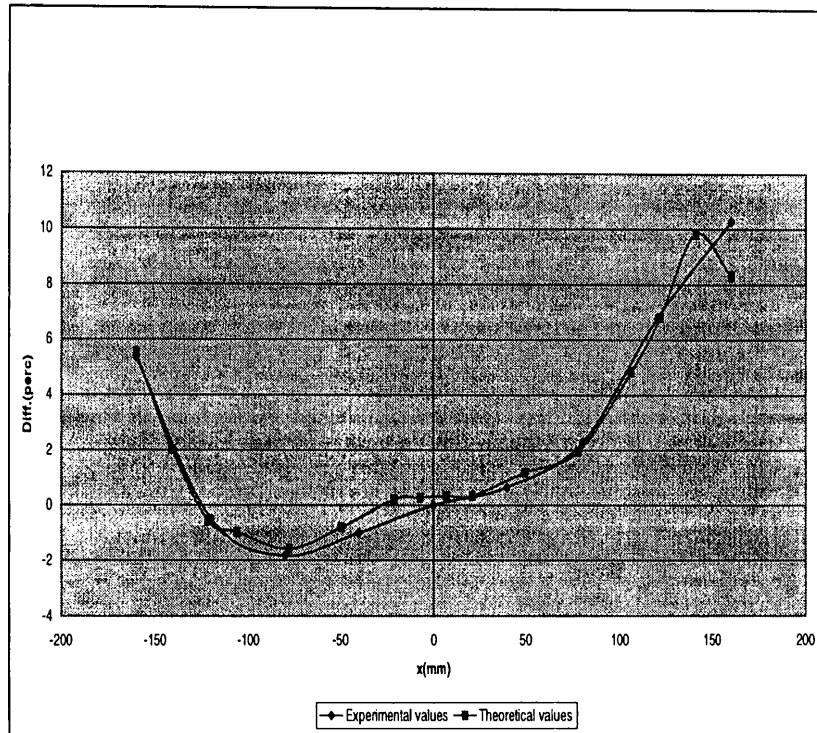
Figure 3: Experimental and theoretical homogeneity curve (I=1000 A) for QD7.

means that all the multipolar components (besides the sextupolar one) are nearly zero. Varing the current (as it is necessary for AD) a finite difference between $\Delta G/G_0$ and $1.462\ x$ shows up and in particular a residual sextupolar component, to be added to the nominal one, is recognizable looking at the slope of the curve around x=0. For x values big enough higer order multipolar components show up that are however little experienced by the cooled beam at low energy.

The difference between model and measurements for I=50 A and I=1000 A is few permille (comparable with experimental errors) whereas for I=2000 A it becomes (for about x > 100 mm) close to 1%. A simple explanation of this could be that close to saturation the two dimensional model gives less accurate results.

The Fourier analysis is based on the fact that the magnetic field in a current free region is
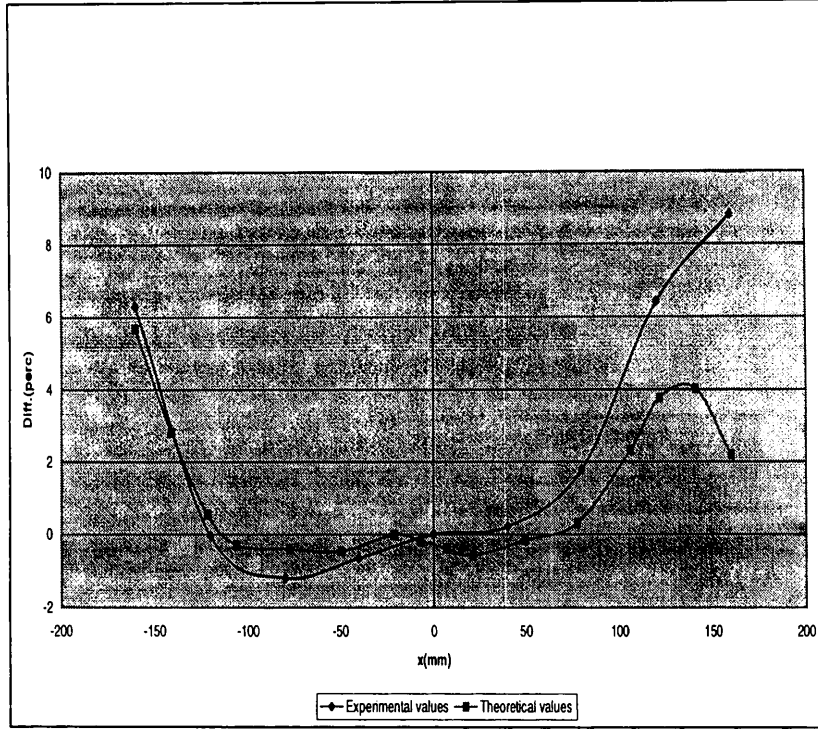
5

Figure 4: Experimental and theoretical homogeneity curve (I=2000 A) for QD7.

an analytic function of complex variable. Therefore the series ($\xi = x + iy = re^{i\theta}$)

$$B(z) = B_y(x,y) + iB_x(x,y) = \sum_{n=1}^{\infty} B_n(\frac{\xi}{R_{ref}})^{n-1} \tag{1}$$

is convergent. The quantity R_{ref} is the reference radius (in our case 80% of the bore radius of the magnet) and the complex coefficients B_n are the multipole coefficients of the expansion; they are connected to the multipolar gradients:

$$G_0 \equiv (\frac{\partial B(\xi)}{\partial \xi})_{\xi=0} = \frac{B(\xi)}{R_{ref}}, \tag{2}$$

$$G_0' \equiv (\frac{\partial^2 B(\xi)}{\partial \xi^2})_{\xi=0} = 2\frac{B(\xi)}{R_{ref}^2}. \tag{3}$$

6

	Measured value	$\sigma = 27\%$	$\sigma = 4\%$
G_0 (T/m)	-4.764	-4.741	-4.77
G_0'/G_0 (m^{-1})	1.462	1.544	1.583

Table 2: QD9: Comparison between the measured and calculated gradients G_0 and G_0'/G_0 at I=1948 A. The results of the calculation are for two different values of the stacking factor σ.

and so on.

To check the reliability of our model concerning the calculation of the high order multipoles (analysis that can be for example used to estimate the influence of the high order resonance on the stability of the motion [11]) we compare the theoretical results for G_0 and G_0'/G_0 with measurements [4].

As shown in tab. 1 the choice of the stacking factor makes a big difference: reducing the B field of 4% respect to the nominal BH curve one gets a good agreement for the quadrupolar gradient but the value of the normalized sextupolar gradient is quite far from the measured one. The contrary happens for a reduction of 27%, as explained above.

2.2 QD9: comparison between 2D model and measurements

For the QD9 no measurements for the low current regime exist and the only available experimental values [1] are those concerning the magnetization curve for I>1000A. As the QD7 and QD9 are identical [5] (the only difference being the number of turns/pole [6]) the measurements on QD7 can be taken as reference point also for QD9.

Fig.(5) shows the good agreeement between the measured magnetization curve and the theoretical one (calculated with a B field reduction of 4% due to stacking factor) while the figs. (6), (7) and (8) reproduce the calculated homogeneity curves.

For the latter we can only point out the fairly good agreement in shape with the measurements on QD7; for the case I=2000 A no saturation effect is visible [6].

Tab. 2 shows the agreement between the calculated values of G_0 and G_0'/G_0 and the nominal ones varying the stacking factor.

It holds what we said about QD7 even if in this case the theoretical values of G_0'/G_0 are both far from the experimental ones.

---

[4]The Fourier analysis has been performed macking use of the program harmo2d [8].

[5]Forgeting about the end shims.

[6]The model for QD9 has been developed introducing a B field reduction with respect to the nominal BH curve of 4%. This makes it problematic to compare the QD7 measurements with the theoretical results for QD9 by means of a simple rescaling.
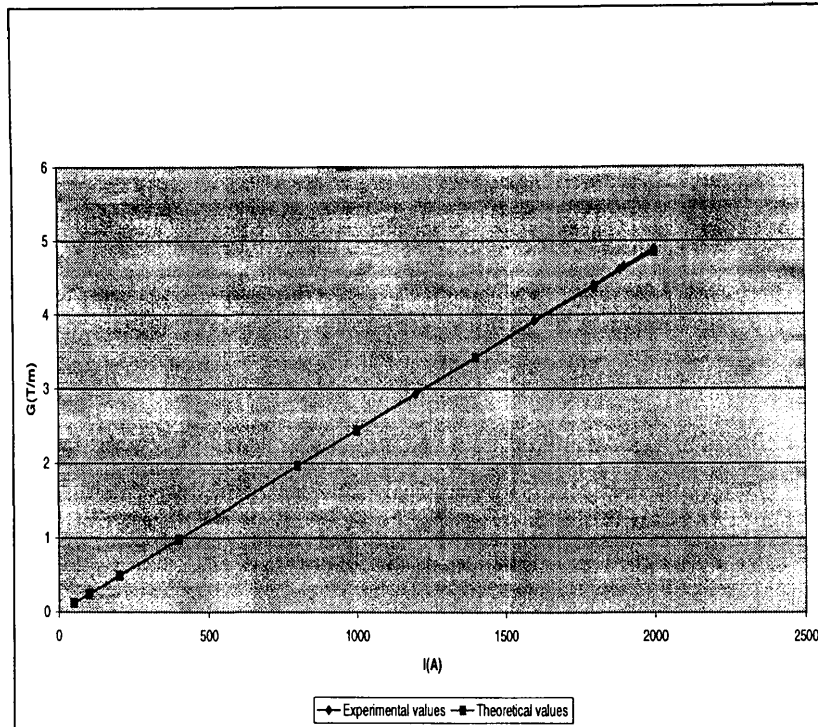
Figure 5: Experimental and theoretical magnetization curve $G_0(I)$ for QD9. The theoretical curve is calculated assuming lamination with stacking factor of 4%.

3   3D analysis

The building up of a 3D model is much more laborius that in the 2D case.

The OPERA 3D preprocessor [4] enables the creation of three dimensional finite element meshes making use of the analysis program TOSCA, ELEKTRA and VF/GFUN. The program has been written to employ a hierarchical data storage system. The finite element mesh is generated by defining the geometry of the three dimensional object projected into a surface (a plane in our case), discretising the projection into finite elements and then extruding it through space to give a 3D model.

The results provided by the program that we are intersting in are those who allow the calculation of the effective length of the two quadrupoles and those who permit to find the integrated octupolar field.
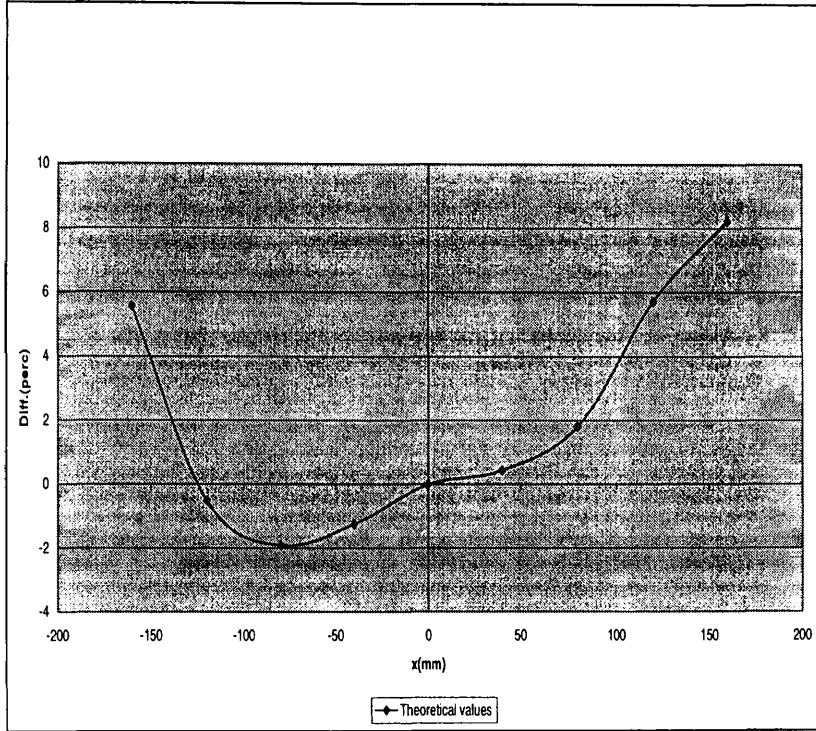
8

Figure 6: Theoretical homogeneity curve (I=50 A) for QD9.

3.1 The effective length of QD7 and QD9

The focal length f of a quadrupol is defined by the relation

$$\frac{1}{f} = kl_{eff} \tag{4}$$

where $k = (q/p)G$ is the strength and

$$l_{eff} = \frac{\displaystyle\int_{-\infty}^{+\infty} G \mathrm{d}z}{G(x,y,0)} \tag{5}$$

is the effective length of the quadrupol.

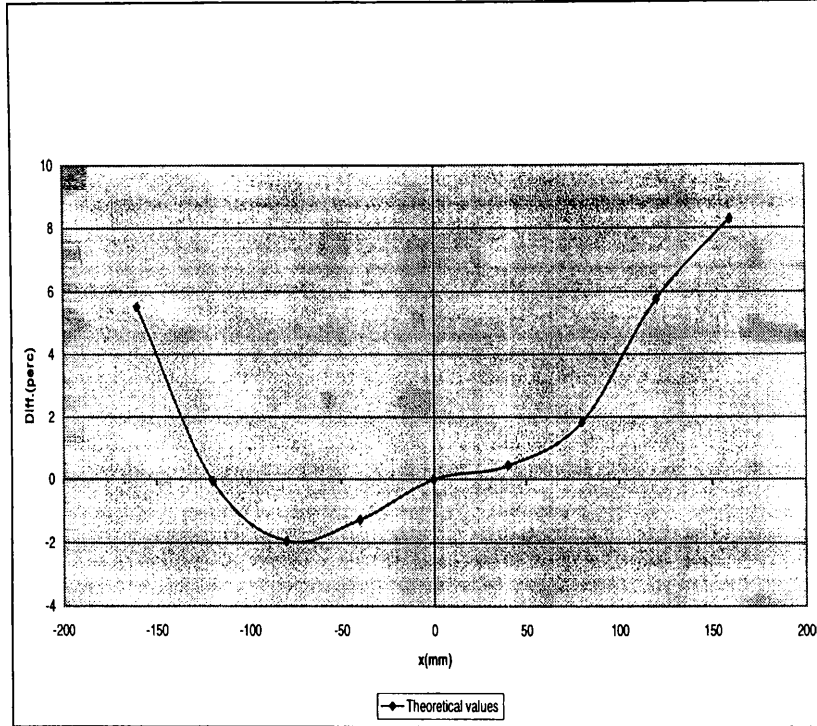In order that the particles of a monochromatic beam are focalized in the same point it is therefore

9

Figure 7: Theoretical homogeneity curve (I=2000 A) for QD9.

necessary that the integral

$$Gl_{eff} = \int_{-\infty}^{+\infty} G(x, y, z)\mathrm{d}z \qquad (6)$$

is constant.

For the exact definition of the effective length we have to compare the theoretical results with

$$l_{eff} = \frac{\displaystyle\int_{-\infty}^{+\infty} G\mathrm{d}z}{G(x, 0, 0)}. \qquad (7)$$

The normalization factor is somehow arbitrary (often the central value of the gradient is used). Empirically the length along which the integral receives a significant contribution is

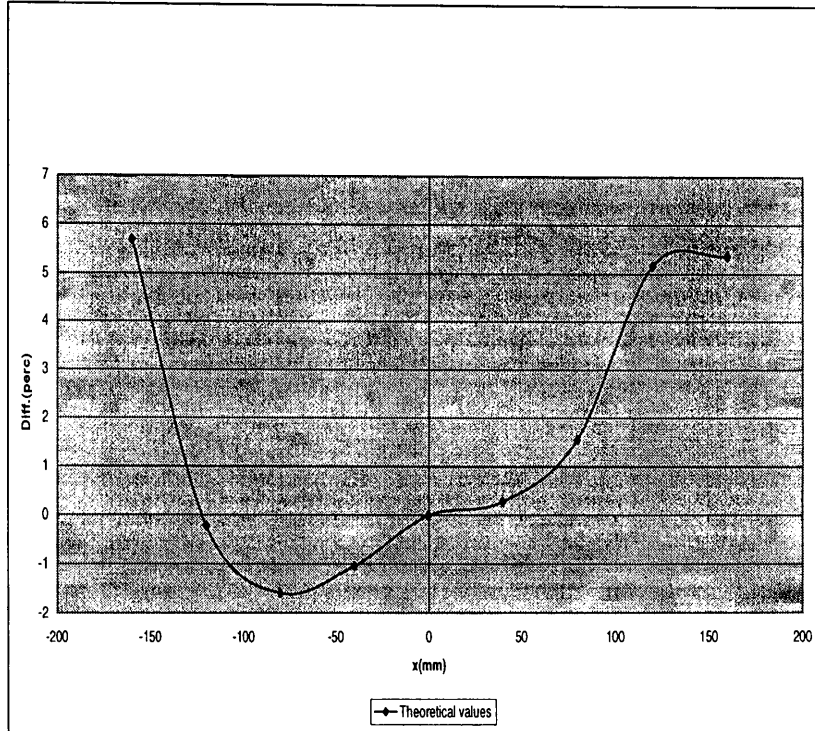$$l \simeq (\text{steel length+8} \cdot \text{bore radius}) \qquad (8)$$

10

Figure 8: Theoretical homogeneity curve (I=2000 A) for QD9.

and an approximate result for l_{eff} is

$$l_{eff} \simeq \text{(steel length+0.8} \cdot \text{bore radius)}. \tag{9}$$

In fig.(9) the good agreement between the theoretical values of the effective length and the measured ones is shown.

Fig.(10) reproduces the analytical results for the effective length of QD9 (for which there are not measurements available); the slope of the curve is in agreement with the measured values for QD7.

The curve $B_y = B_y(x)$ (used to calculate the quadrupolar gradient) for the QD7's model shows a pronounced and unexpected spike around the origin that does not allow the calculation of the effective length for $x = 0$ (see fig. 9). The same problem has been found during the modelization of QD9 but, refining the mesh, we were able to get a curve much more regular then for QD7. In fact in this case the calculated effective length for $x = 0$ is in agreement (see fig. 10) with the other points of the curve.
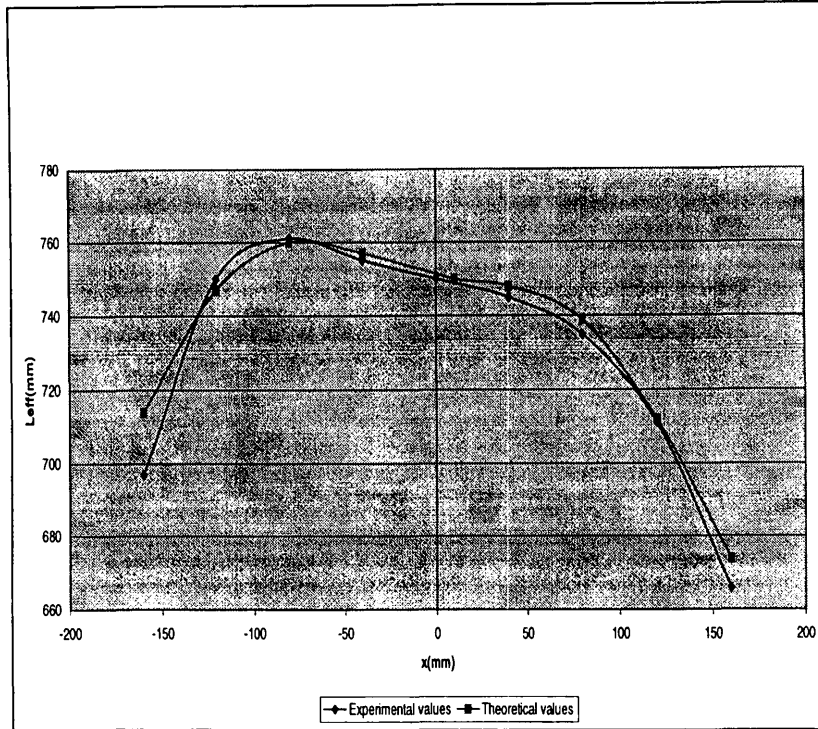
11

Figure 9: Effective length of QD7 as function of the horizontal coordinate.

4 Analysis of the octupolar field

The aim is now the evaluation of the octupolar gradient $G_2(0, 0, z) = (\dfrac{\partial^3 B_y}{\partial x^3})$ along the z-axis in order to estimate the strength of the pseudo octupolar field and the value of the real octupolar component in the center of the magnet. Fig. (11) and (12) show the curves $G_2 = G_2(z)$ for the two models.

4.1 The pseudo octupolar field

The so called pseudo octupolar field is the additional field component due to the frienge field (that is due to the dependence of the quadrupolar gradient on the longitudinal coordinate z). It
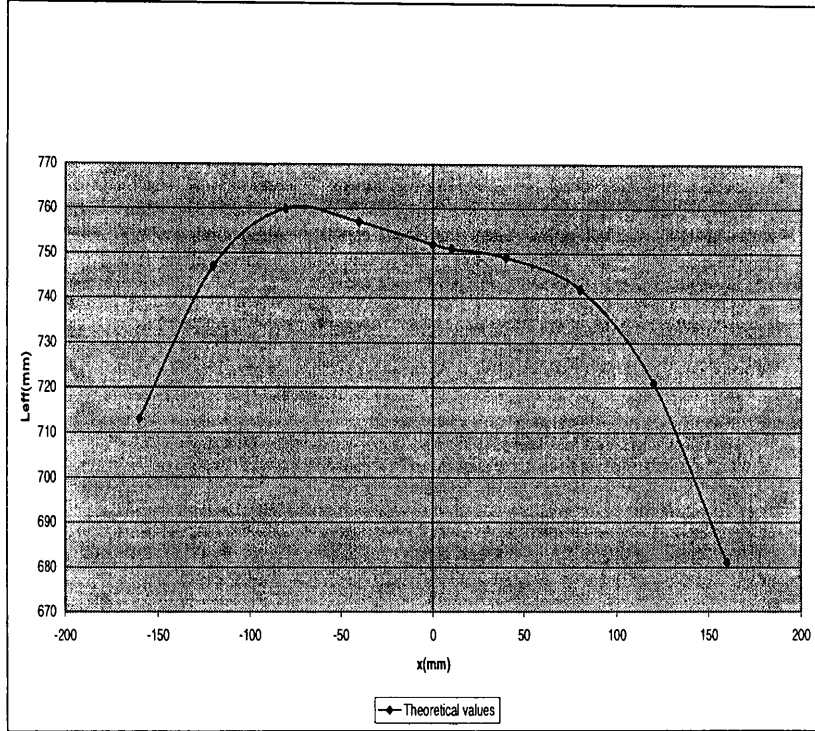
Figure 10: Effective length of QD9 as function of the horizontal coordinate.

can be expressed [9] as

$$
\begin{cases}
B_x = \dfrac{1}{12}G''y^3 + \dfrac{1}{4}G''x^2y \\[2mm]
B_y = \dfrac{1}{12}G''x^3 + \dfrac{1}{4}G''xy^2 \\[2mm]
B_s = G'xy
\end{cases}
\tag{10}
$$

where $G'' \equiv \dfrac{\partial^2 G}{\partial z^2} = -2\dfrac{\partial^3 B_y}{\partial x^3}$.

This field affects the chromatic behaviour of the tunes. Following [5] we tried in [10] to reproduce by means of it the parabolic shape of $Q_x = Q_x(\Delta p/p)$ measured in the AC. For this purpose we made use of a model proposed by P. Krejcik in [5].

Now we are able to compare the hypothesis on which this approach is based with the results
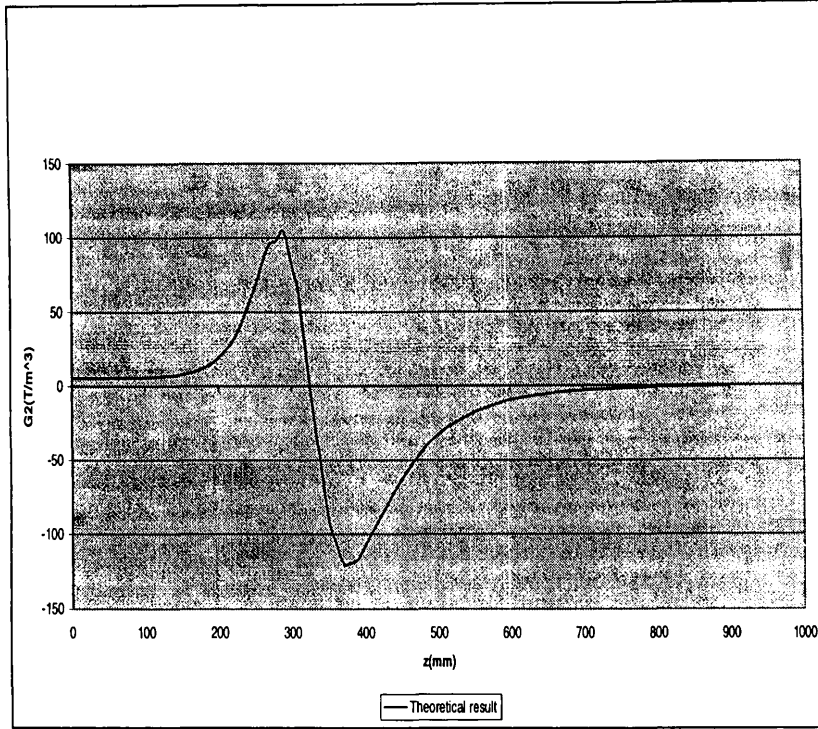
13

Figure 11: Dependence of the octupolar gradient on the longitudinal coordinate for QD7.

provided by the two models.
Assuming $G_2(z)$ as a quadratic function of z [5]:

$$G_2(z) = (\frac{\partial^3 B_y}{\partial x^3})_{(0,0,z)} = a_1 + a_2 z + a_3 z^2 \tag{11}$$

and calling a the length along which the gradient rises from zero to half of the value in the center of the magnet (G_0) [7] one finds (fig. (13)):

$$G_2(z) = G_0(-\text{sign}(z)\frac{z^2}{2a^2} + \frac{z}{a} + \frac{1}{2}) \quad (|z| \leq a) \tag{12}$$

---

[7]In [5] a is assumed to be equal to the bore radius of the quadrupole.
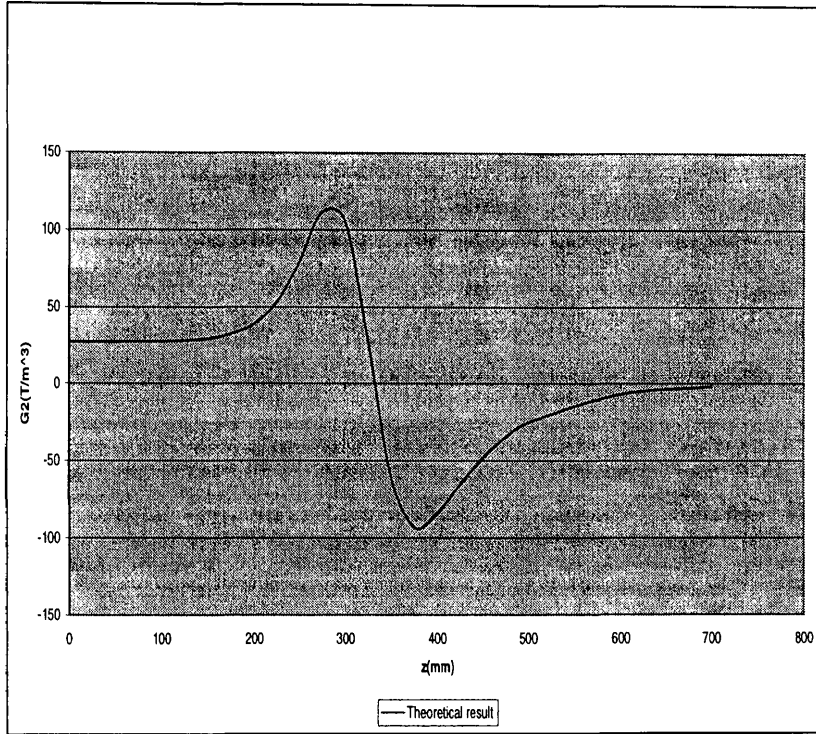
14

Figure 12: Dependence of the octupolar gradient on the longitudinal coordinate for QD7.

where

$$\text{sign}(z) = \begin{cases} -1 & \text{if } z < 0 \\ 1 & \text{if } z \geq 0. \end{cases} \tag{13}$$

From (12) we get (fig. (14))

$$G'' = -\text{sign}(z)\frac{G_0}{a^2}. \tag{14}$$

As shown in [5,10] [8], according to this result the chromatic effect of the pseudo octupolar field can be rappresented by placing at the two ends of each quadrupole a thin quadrupolar lens

---

[8]The two final result in [5] and [10] are slightly different: in [5] the factor $a(x_0')^2$ in (15) is replaced by $2a(x_0')^2$ for reason which we do not understand. Anyway the ratio $(2)a(x_0')^2/x_0x_0'$ is about 10^{-2} and the term $(2)a(x_0')^2$ can be in first approximation neglected
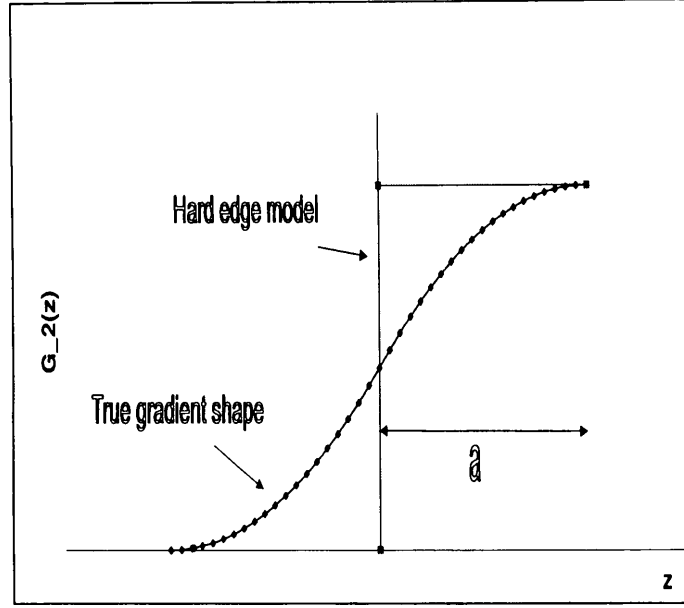
15

Figure 13: Gradient end-shape according to the pseudo octupolar model used in [5].

whose matrix is

$$(M)_{tl} = \begin{pmatrix} 1 & 0 & 0 & 0 \\ \mp\dfrac{K_0}{2}[x_0 x_0' + a(x_0')^2] & 1 & 0 & 0 \\ 0 & 0 & 1 & 0 \\ 0 & 0 & \pm\dfrac{K_0}{2}(x_0 x_0') & 1 \end{pmatrix} \tag{15}$$

(the sign "-" holds for the entrance and the sign "+" holds for the exit). where x_0 and x_0' are, respectively, the position and the angle of the particle at the begining of the region in which the pseudo-octupolar field is present.

The important quantity to be evaluated is the area under the positive and the negative part of the curve $G_2(z)$. In absence of any other (real) octupolar component the two areas, by virtue of Maxwell's equation, should be equal.

The value predicted by the Krejcik's model is

$$\int_0^a \frac{\partial^2 G_2}{\partial z^2} ds = \int_0^a \frac{G_0}{a^2} dz = \frac{G_0}{a} \tag{16}$$
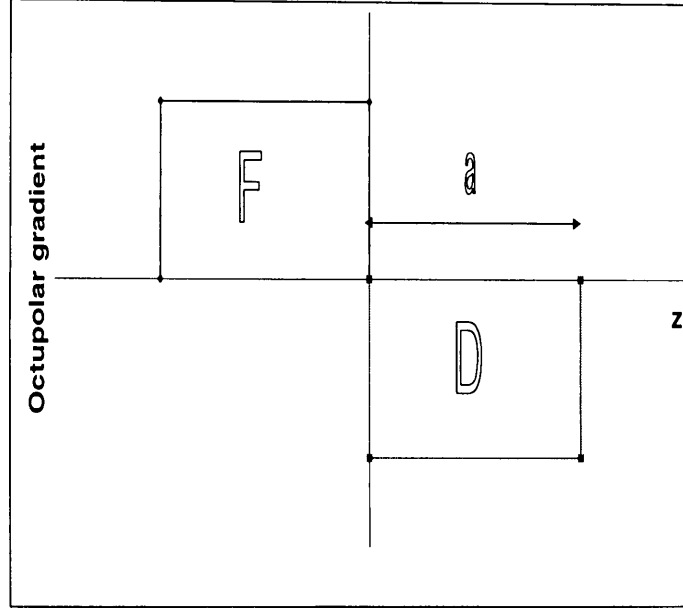
16

Figure 14: Second derivative of the gradient according to Krejcik's model of the pseudo octupoles.

For the two areas we define the ratio with respect to Krejcik's value as:

$$\alpha_\pm = \frac{2\int \frac{\partial^3 B_y}{\partial x^3}\mathrm{d}z}{\int_0^a \frac{\partial^2 G}{\partial z^2}\mathrm{d}z} = \frac{2\int \frac{\partial^3 B_y}{\partial x^3}\mathrm{d}z}{G_0/a} \tag{17}$$

where the integral of B_y is calculated by numerical integration of the curves (11) and (12) and is extended either to the positive area (α_+) or to the negative one (α_-). Following Krejcik we take for a the bore radius.

For the QD7 we found the results

$$\alpha_+ = \frac{17.73\ \mathrm{T/m^2}}{46.47\ \mathrm{T/m^2}} = 0.38; \quad \alpha_- = \frac{16.12\ \mathrm{T/m^2}}{46.47\ \mathrm{T/m^2}} = 0.35. \tag{18}$$

According to this result Krejcik's model seems to overerstimate the pseudo octupolar effect by more then 60%. This values is affected by the irregular spike around the origin of the curve

17

	Peak to peak (mm)	Zero position (mm)
Model	132 (=bore radius)	370 ($=l_{eff}/2$)
QD7	110	330
QD9	100	340

Table 3: Comparison between the values of the distance peak to peak and of the zero position in the curve giving the dependence of the pseudo octupolar gradient on the longitudinal coordinate (see fig. (11) and 12): as assumed in the Krejcik's model and as provided by the 3D simulations for QD7 and QD9.

$B_y = B_y(x)$ (see paragraph 3.1): to fit this curve so as to get $\dfrac{\partial^3 B_y}{\partial x^3}$, we had to remove the spike and the number of points removed influences the result. The criterion we used is the following: the number of removed points is such that the coefficient of the first order term in the third order polinomial fitting the curve $B_y = B_y(x)$, that is the quadrupolar gradient, is as close as possible to the experimental value [6].

An other important information we draw from this comparison is that, since $\alpha_+ \neq \alpha_-$, the field generated by the quadrupole contains a real octupolar component.

This is even more evident considering the result for QD9:

$$\alpha_+ = \frac{31.15 \text{ T/m}^2}{36.09 \text{ T/m}^2} = 0.86; \quad \alpha_- = \frac{23.43 \text{ T/m}^2}{36.09 \text{ T/m}^2} = 0.65. \tag{19}$$

Here the difference between α_+ and α_- is significant. This comes also out from fig. (11) and fig. (12).

As we pointed out in paragraph 3.1 the QD9 model is almost not affected by the irregular peak in the curve $B_y = B_y(x)$ and this makes the result (19) more reliable.

A further comparison between the value of two characteristic parameters of the Krejcik's model and the results of the 3D simulations is shown in tab. 3.

4.2 The real octupolar field

As we have shown, the 3D simulations of the QD7 and QD9 indicate the presence of an additional integrated octupolar component that has to be taken into account for evaluating the chromatic behaviour of the AC (AD)'s tunes (in addition to the pseudo octupoles due to stray field).

To check to what extent our results are in agreement with the intention of the designers we have to consider that they projected the W quadrupoles so as to create an octupolar gradient [9] that can be in principle compensated (in sense that the total integrated octupolar field can be adjusted to zero) by means of end-shims and "washers" placed on them.

This two end effects are not included in our models and all what we can expect is that the values

---

[9]Apart from the inevitable pseudo octupolar contribution.

of the octupolar field is inside or not too far outside the variation range given in [1].
The measured variation range for the octupolar strength generated by QD7 is

$$-1.5 \text{ m}^{-4} < [(K_3)_{z=0}]_{QD7} < 1.5 \text{ m}^{-4} \tag{20}$$

whereas the one for QD9 is

$$-1.2 \text{ m}^{-4} < [(K_3)_{z=0}]_{QD9} < 1.2 \text{ m}^{-4}. \tag{21}$$

On the basis of the 3D simulations discussed in the previous paragraph we have found for QD7

$$(G_3)_{z=0} \equiv (\frac{\partial^3 B_z}{\partial x^3})_{z=0} = 5.539 \text{ T/m}^3. \tag{22}$$

The nominal energy for AC is $p = 3.57432$ GeV/c and so the octupolar strength corresponding to $(G_3)_{z=0}$ is

$$(K_3)_{z=0} = \frac{1}{B\rho} \text{ [Tm]}(G_3)_{z=0} = \frac{1}{0.2998}p \text{ [GeV/c] } (G_3)_{z=0} = 0.4650 \text{ m}^{-4}. \tag{23}$$

Anagously for QD9

$$(G_3)_{z=0} = 27.068 \text{ T/m}^3 \quad \rightarrow \quad (K_3)_{s=0} = 2.27190 \text{ m}^{-4}. \tag{24}$$

The value provided by the model of QD7 is in good agreement with measurements while the result for QD9 can be considered accettable. In fact the variation range is only referred to every possible different configuration of the "washers" and the extreme values take already into account the effect of the end-shims that presumably reduce them with respect to the case in which only the field generated by the "body" of the magnets is considered (that is the case of our model). Moreover the measurements refer in both case to the nominal current I=1884.8 A whereas our models are calculated for I=1948 A [1]. The value of K_3 varies (not linearly) with the current and the value for I=1948 A is biger (of few percent) than the one at I=1884.8 A.
Even if we do not have any informations about the octupolar field generated by the family of QWF6, it is possible to get it by interpolation of the values of K_3 for QD7 and QD9 and this because QD7, QD9 and QF6 are identical, the only difference being the number of Ampere/turnes [6].
The fact that the working point of these quadrupoles is close to the saturation would suggest a parabolic interpolation but, since we know only two points of the curve giving the dependence of K_3 respect to the number of Ampere/turnes, we have to be satisfied with a linear one. Following this way we found for QF6:

$$(K_3)_{(z=0)} = 1.514 \text{ m}^{-4}. \tag{25}$$

The family of QF8 is not identical to the other three W ones [6] and so it is not possible to extract information about the octupolar field from the models developed. On the other hand the QF8 quadrupoles are less asymmetric and so we can expect a weaker value of the octupolar gradient.
Concerning the narrow quadrupoles we can assume that, due to their symmetry, they do not generate any real octupolar field.
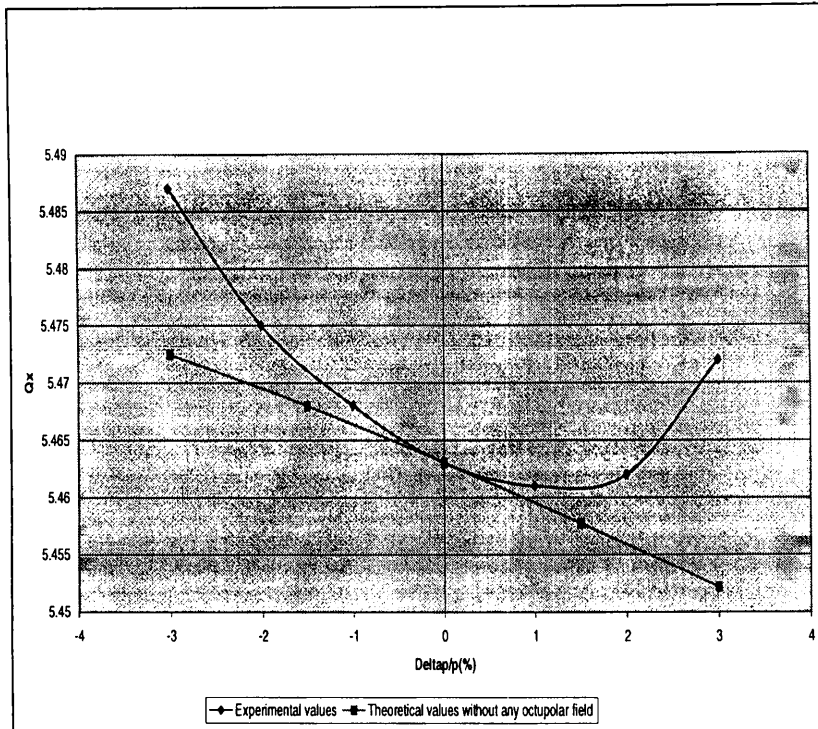
Figure 15: Experimental and theoretical chromatic behaviour of Q_x for the AC do not taking into account any octupolar field.

5 Chromatic behaviour af the AC's tunes

Our final aim is to exploit the calculations presented in the previous paragraphs on the octupolar (real an pseudo) field generated by the W quadrupoles to try to improve (respect to [10]) the agreement with the measurements concerning the dependence of the AC's tunes on the momentum deviation $\Delta p/p$.

Fig. (15) and (16) show the difference between experimental and theoretical values not taking into account any octupolar field in the calculations. While the agreement is quite good for the vertical plane, the horizontal tune shows a parabolic shape that is not forseen by the theoretical curve.

In [10] we have shown that the insertion of the pseudo octupolar field following the Krejcik's model improves in a significant way the agreement for Q_x.

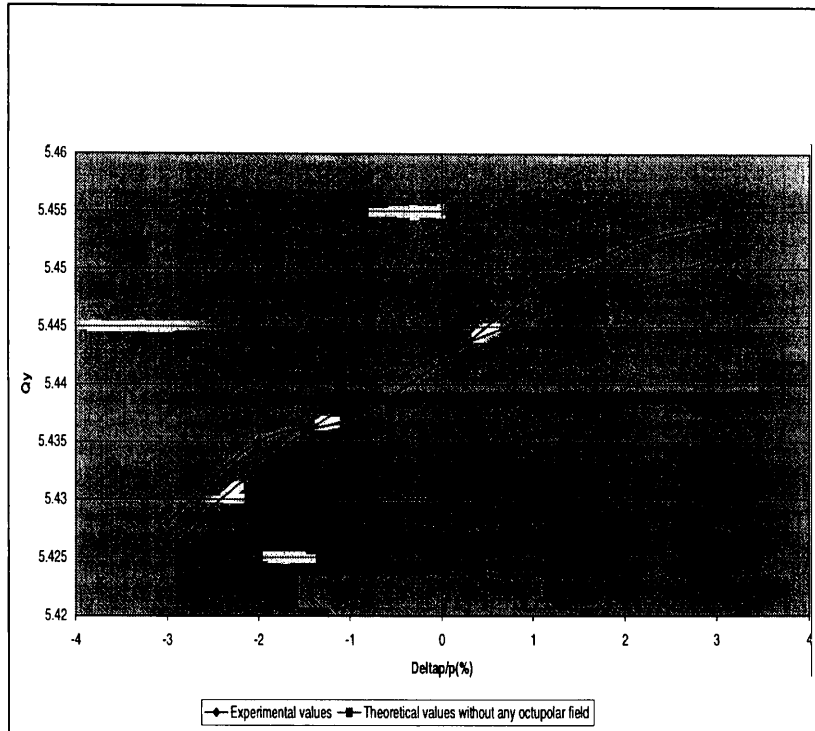However according to the calculation performed, the pseudo octupolar field should be reduced

Figure 16: Experimental and theoretical chromatic behaviour of Q_y for the AC do not taking into account any octupolar field.

considerably.

In figs (17) and (18) a comparison between the experimental chromatic curves and calculations adding either real and pseudo octupoles or real and the half pseudo octupoles is shown for both planes.

Concerning the real octupolar field, we inserted it in our model by means of one thin lens placed in the center of each W quadrupol (except for the QF8 family) and characterized by a strength equal to the one we found in paragraph (4.2). This means that for simplicity we neglected the effect of the end shims (as well as of the "washers") assuming the same value of the octupolar gradient for each quadrupol inside the same family.

In the horizontal plane the agreement between measurements and theoretical curve adding real and half pseudo octupoles is quite good while the curve with the full effect of the pseudo octupoles is a little overestimating.

In the vertical plane the insertion of the octupolar effect makes the agreement worse; the shape
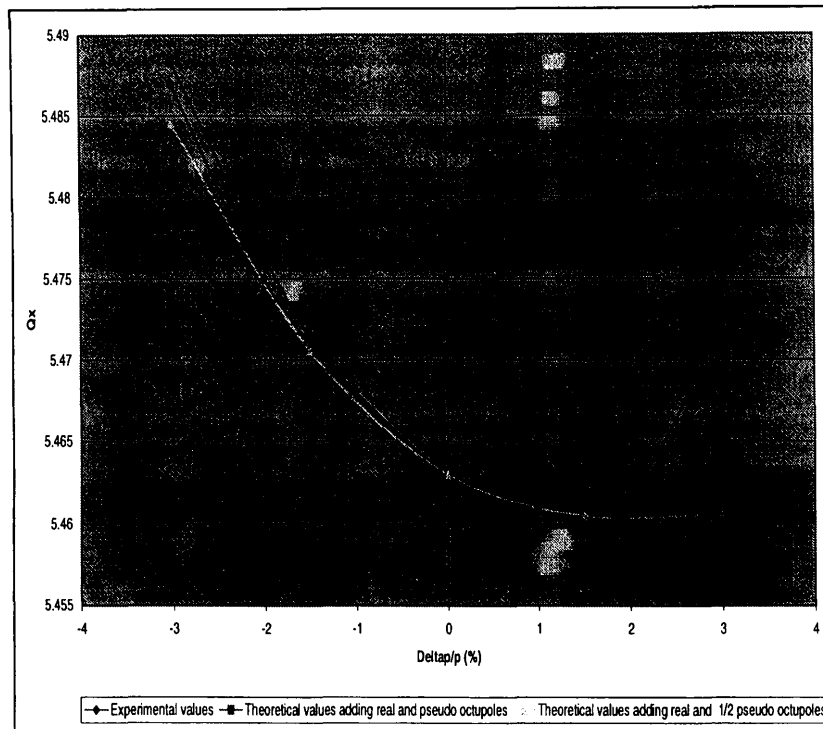
21

Figure 17: Experimental and theoretical chromatic behaviour of Q_x for the AC taking into account the real and pseudo octupolar field.

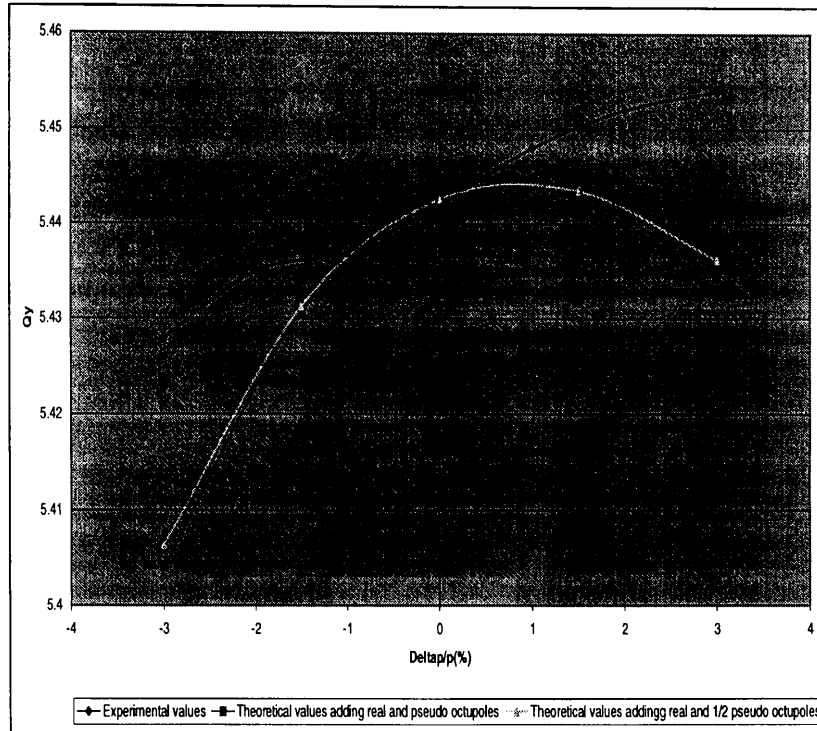of the experimental curve seems in this case hard to modelize.

Figure 18: Experimental and theoretical chromatic behaviour of Q_y for the AC taking into account the real and pseudo octupolar field.

Conclusions

In this work we compared the results provided by 2D and 3D simulations performed on a couple of AD (AC) quadrupoles with measurements.

The 2D models is quite sensitive to the choice of the staking factor. While the experimental homogeneity and magnetization curves are fairly reproduced, the Fourier analysis does not fit in a satisfactory way with the nominal (measured) gradients.

The 3D analysis is affected in both cases by an unespected spike (more important for QD7 than for QD9) around the origin of the curve $B_y = B_y(x)$ that is the starting point of all our calculations. In spite of this the curves of the effective length are in good agreement with measurements and also the analysis of the pseudo and real octupolar field seem to be reliable.

According to these calculations we can conclude that the Krejcik's model used to introduce the

23

pseudo octupolar effect in the dependence of the AC's tunes on the momentum overestimates it of about 50%.

This result is also in agreement with the experimental evaluation of the psedo octupolar field made for one LEAR quadrupol [9].

The real octupolar field is produced because the asymmetry of the two quadrupoles and can be controled by means of a set of "washers" placed on the end shims of each W quadrupol. We have shown in [10] that the pseudo octupolar effect can be compensated by a real octupolar field, this also means that it will possible to use a good choice of the configuration of the "washers" to cancel (or at least to reduce) the pseudo octupoles in AD.

The attempt to improve the agreement between the experimental chromatic behaviour of the AC's tunes and the theoretical calculations can be considered succesfull for the horizontal plane. For the vertical one, maybe because the particular configurations of the "washers" (not taken into account in our calculations), the experimental curve does not show the strong octupolar influence suggested by the calculations.

Acknowledgements

References

1. Ph. Cartier, E. Chinchio, G. Suberlucq, *Pricipaux parameters des aimants mesures et testes par le groupe PSR. Table des aimants d'ACOL*, not pubblished (1987).

2. D. Cornuet, Private communication.

3. *OPERA-2d Reference Manual*, VF-11-94-24 (1994).

4. *OPERA-3d Reference Manual*, VF-11-93-D4 (1993).

5. P. Krejcik, *Non linear quadrupole end-field effects in the CERN antiproton accumulators*, Proceedings of the 1987 IEE Particle Accelerator Conference, Washington 1987, pp.1278-1280.

6. H. Koziol, S. Maury, *Parameter list for the Antiproton Accumulator Complex (AAC)*, CERN/PS 95-15 (1995).

7. L. Rinolfi, Private communication.

8. G. Borri, Private communication.

9. E. Gianfelice, D. Mohl, *On fourth order resonances in machines with strongly varying focusing functions*, CERN/PS/LEA 84-3 (1984).

10. G. De Ninno, *The pseudo-octupolar effect in the AC and AD rings*, PS/HP 97-33 (1997).

11. P. Belochitskii, Private communication.

12. D.C. Carey, *The optics of charged particle beams*, Harwood academic pubblishers (1986).

13. H. Grote, F.C. Iseline, *The MAD program, User's Reference Manual*, CERN/SL/90-13 (1990).

Low Energy Beam Transport line for ASCUSA experiment in the AD project

F. Grandclaude and A. Lombardi

Introduction

This note intends to give an overview of the Low Energy Beam Transport located behind the AD-RFQ. The purpose of the LEBT is to transport and focus the antiproton beam coming out from the AD-RFQ to the ASACUSA experiment:

- For phase 2: beam transport to the vacuum window of the gas-target experiment. The beam must be at a waist to have a spot size as little as possible over the longitudinal length of the gas target;
- For phase 3: beam transport to the trap located in the middle of the super-conducting solenoid. The transversal beam size must be also as little as possible, because only particles within ±1 mm from the longitudinal axis z can be used for the experiment. Moreover, the temporal length of the beam must be shorter than the shutter time of the trap, in order not to lose particles longitudinally.

Beam coming out from the AD-RFQ

Fig. 1 and Table 1 shows the transversal beam characteristics at position $z=0$, corresponding to the AD-RFQ inside wall. The simulations were made with 1000 particles coming out from the AD ring.
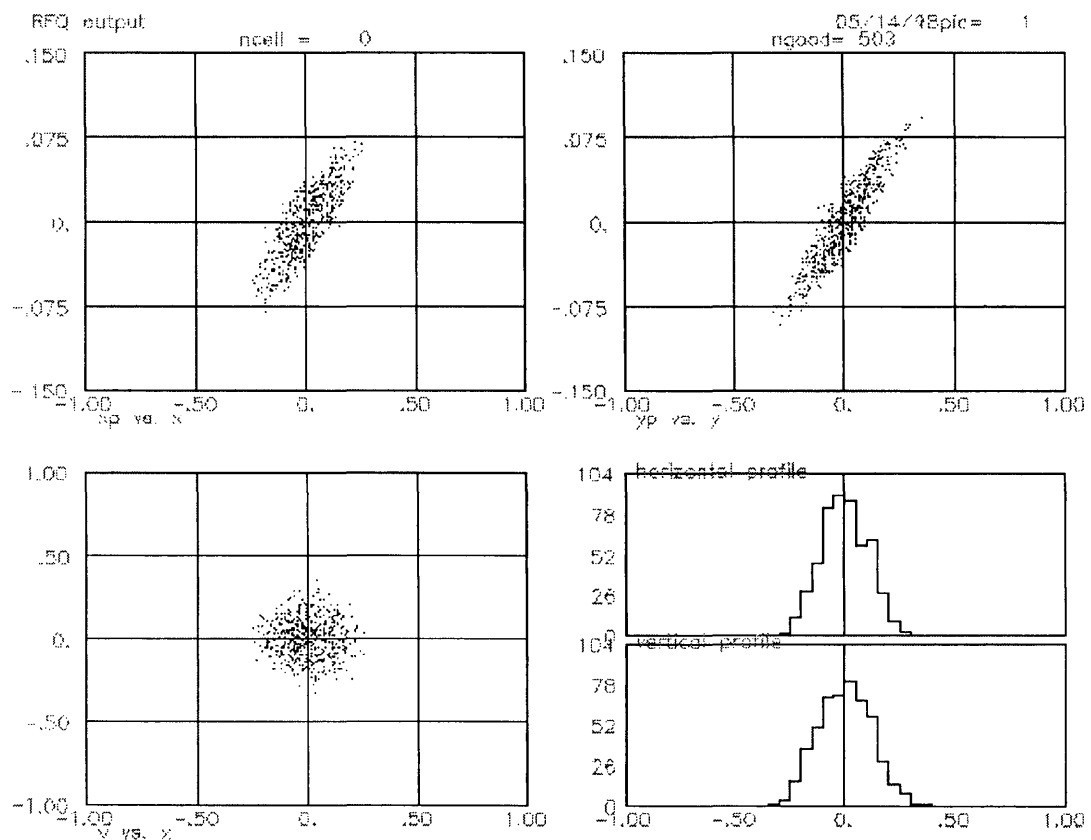

Fig. 1: Beam at output of AD-RFQ (position in cm, divergence in rad)

Particles coming out from the RFQ have an average energy of 63.3 keV, and the total physical emittance of the beam is ~100 mm.mrad. This is for a total physical emittance of 10 mm.mrad at the beginning of AD-RFQ, a value that represents an effective overall emittance, taking into account the surface in phase space covered by the beam over successive shots.

At the output of the RFQ, 50% of the particles are in the useful energy range, namely (60±10) keV, as pointed out in Table 1 (503 particles at output of RFQ for 1000 particles coming out from the AD ring)

Numb of particles	plane	Emittance, cm.mrad (normalised)			alpha	Beta(u)
		100%	90%	rms(n)		cm/mrad
503	x-xp	0.1728	0.0889	0.0215	-1.391	0.005679
	y-yp	0.2187	0.0877	0.0213	-2.184	0.007803

Table 1: Emittance and Twiss parameters of the beam coming out the AD-RFQ.

Layout of the LEBT for phase 2

With three quadrupoles

The first idea was to transport the beam through three existing magnetic quadrupoles, until the formvar window, with the first quadrupole inside the RFQ cover. Fig. 2 shows the beam envelope through the LEBT:
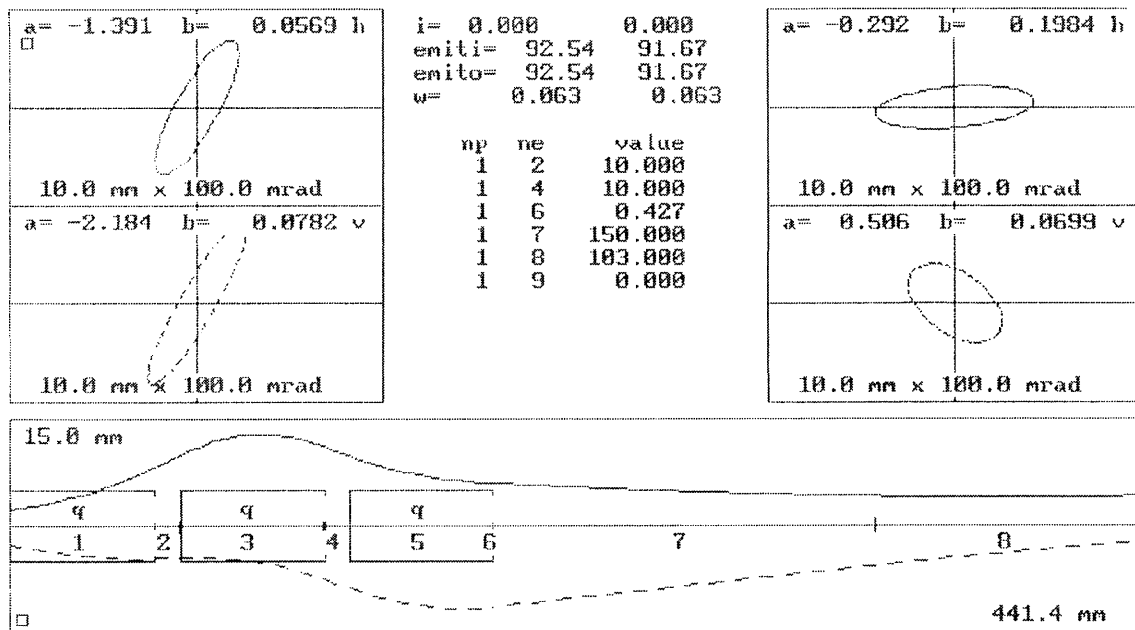

Fig. 2: Beam envelope in the LEBT composed of three quads (top: x plane; bottom: y-plane)

Specifications for the quadrupoles:

	Q1	Q2	Q3
Length (mm)	56	56	56
Internal diameter (mm)	29	29	29
External diameter (mm)	113	113	113
Magnetic field gradient (T/m)	-15	+16.5	-10
Magnetic Field (kG)	-4.35	+4.785	-2.9

(a positive sign means that the magnetic field is horizontally focusing)

The space between each quadrupole is 10 mm. A free space of 253 mm is reserved for the vacuum valve and a beam diagnostic device.

The advantage of this "triplet" solution is to provide a round beam at the formvar window, if this is not the case at the output of the AD-RFQ. With this configuration, we achieved a final spot size at the formvar window of 10 mm (diameter, 5 rms). Fig 3 and Table 2 below show the results of multi-particles simulation done with PATH-TRAVEL.
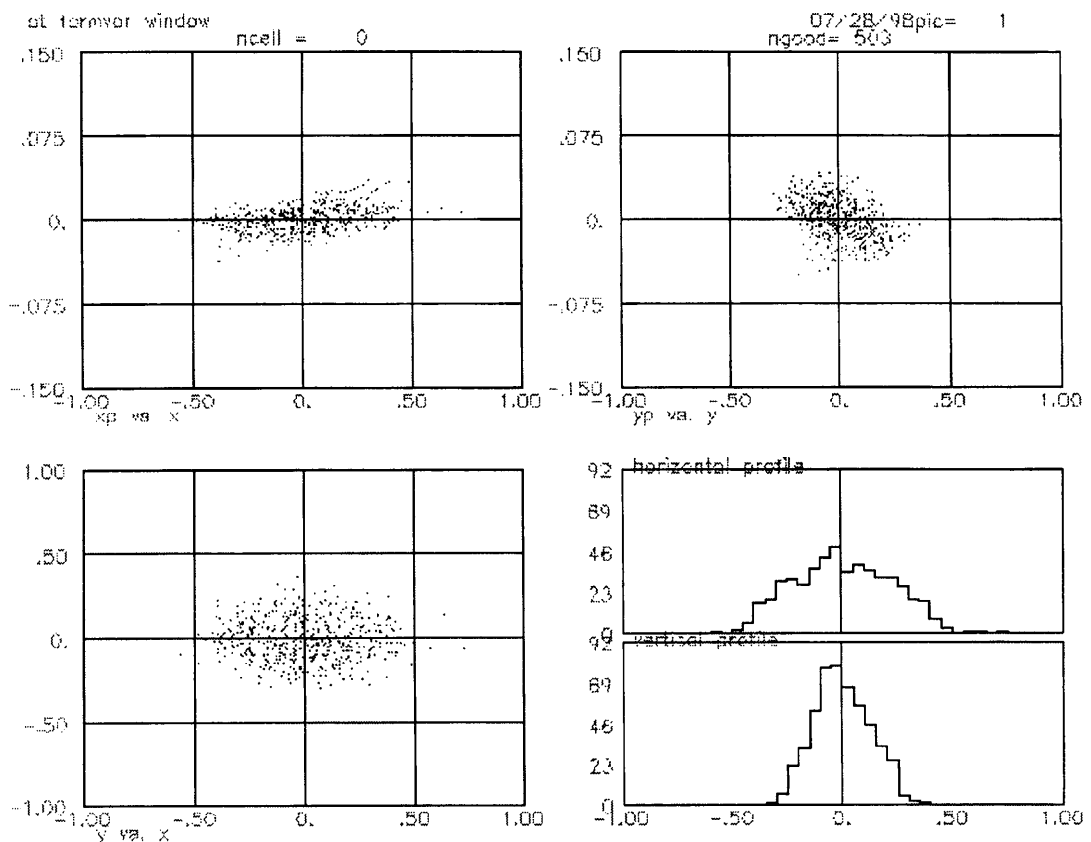

Fig. 3: Beam at formvar window - triplet solution (position in cm, divergence in rad)

Numb. of particles	Plane	emittance, cm.mrad (normalised)			Alpha	beta(u)
		100%	90%	rms(n)		cm/mrad
503	x-xp	03024	0.1106	0.0252	-0.440	0.023163
	y-yp	0.3557	0.1016	0.0237	0.468	0.007815

Table 2: Emittance and Twiss parameters of the beam at formvar window.

With a solenoid

Actually, a much smaller transversal size of the beam (4.9 mm diameter, 5 rms) has been achieved by using a RFQ2-type solenoid (135 mm effective length, 30mm bore radius with a longitudinal field of 6.65 kG — 985 Amps). See Fig. 4 & Fig. 5 below:
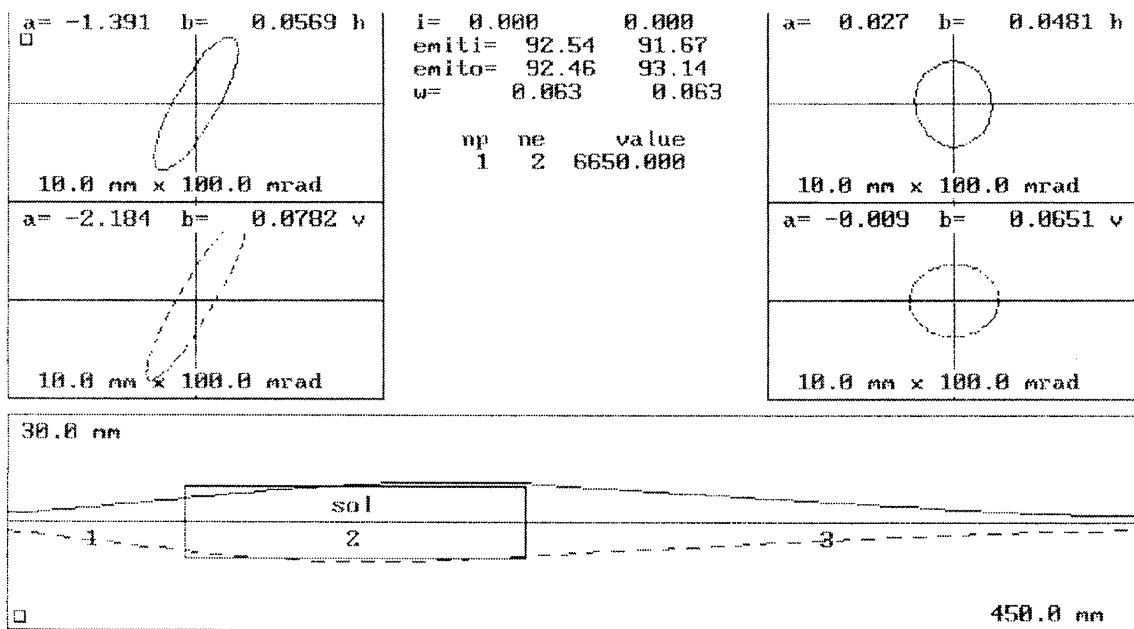

Fig. 4: Beam envelope in the LEBT composed of RFQ2-type solenoid (top: x plane; bottom: y-plane)
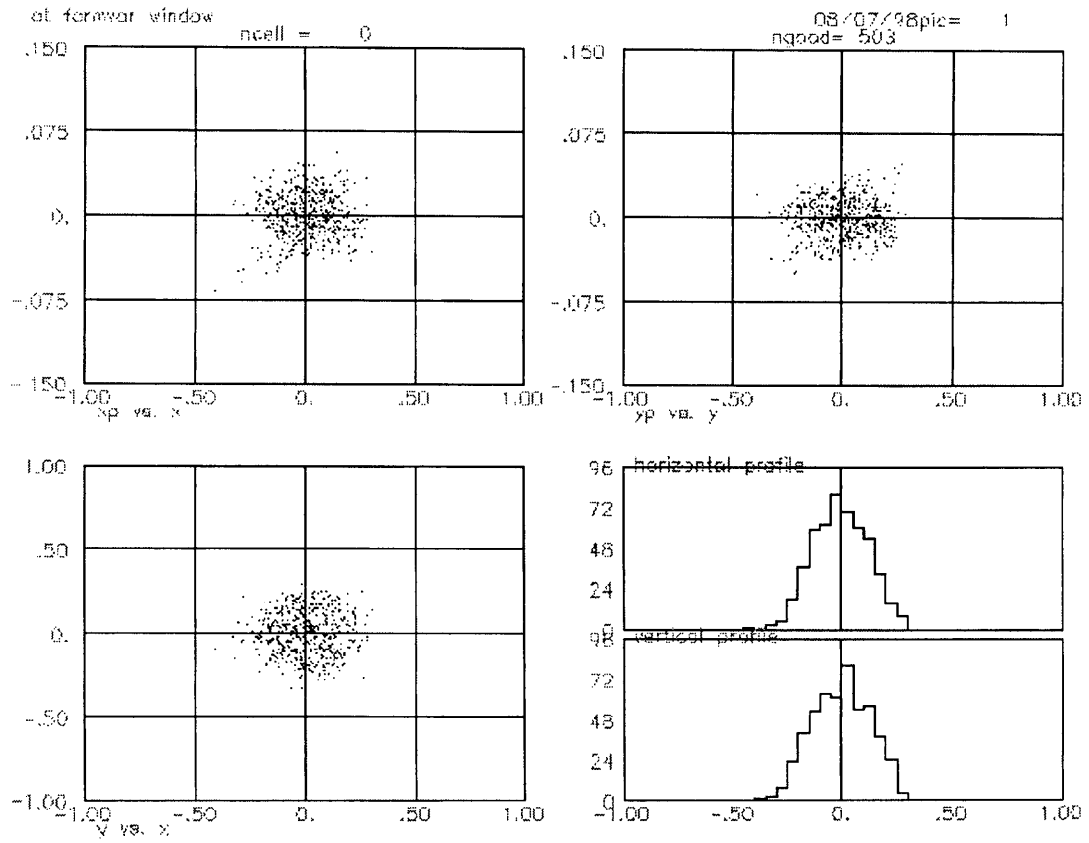
Fig. 5: Beam at formvar window - solenoid solution (position in cm, divergence in rad)

Layout of the LEBT for phase 3

The AD-RFQ decelerates the particles to (60 ± 10) keV. Due to this energy spread, the beam tends to get longer *in time* along its propagation (see Fig. 6).
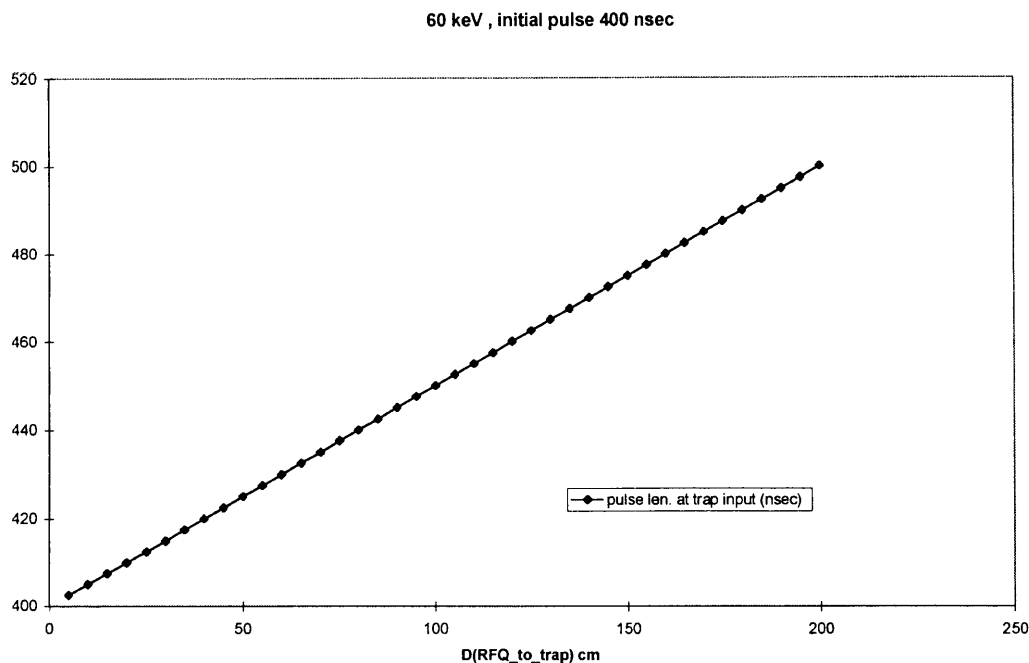
60 keV , initial pulse 400 nsec

Fig. 6: Pulse length (nsec) at trap input for (60±10) keV energy out of the RFQ versus distance RFQ to trap.

For the first case we have investigate below (Super-conducting solenoid located just behind the RFQ), this elongation in time has no influence on the capture efficiency, because the shutter time of the trap for an energy of 60 keV is still longer than the duration of the beam. However, putting a degrader foil may help to reduce the transversal beam size.

But for the second case (Super-conducting solenoid located behind the phase 2 LEBT), the distance between the output of the RFQ and the trap may lead to a temporal length of the beam *greater than* the shutter time of the trap for an energy of 60 keV. A degrader foil is therefore necessary to decrease the energy to some tens keV, in order to increase the shutter time of the trap.

Moreover, decelerating the anti-protons simplifies their longitudinal capture in terms of voltage power supplies: without a degrader foil, a voltage of ~60 kV should be applied on both end of the trap, but with it, reducing the energy to 10 keV, only 10 kV are necessary.

Super-conducting solenoid located just behind the RFQ

The simplest and the more space-saving solution was to put the super-conducting (SC) solenoid just behind the AD-RFQ.

In our simulations, particles are taken from the output of AD-RFQ at beginning of RFQ cover, then transported through a 5 cm drift corresponding to the RFQ cover, and finally in the first half of the solenoid which is one meter long. The simulation of the particles dynamic was made using the field map of the SC solenoid provided by its manufacturer.

The envelope of the beam inside the first half of the SC solenoid (Fig. 7) suggested to put a degrader foil at the point where the beam size is minimum (z=305 mm here), in order to further reduce it at the trap.
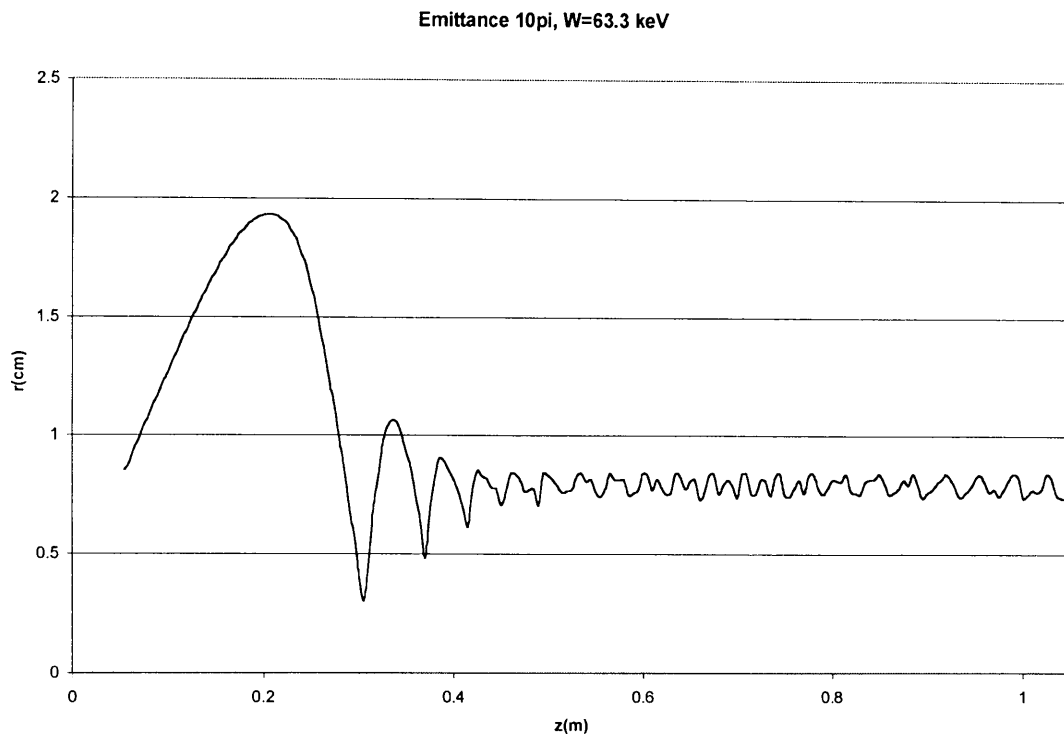
Emittance 10pi, W=63.3 keV

Fig.7: Beam envelope in the first half of the SC solenoid (z=0 corresponds, in the whole document, to AD-RFQ inside wall).

With this simple set-up, the 5*rms diameter of the beam at the trap center is 9.6 mm (15.8 mm taking into account all the particles, see Fig. 7).

Numb. of particles	Plane	emittance,cm.mrad (normalised)			Alpha	beta(u)
		100%	90%	rms(n)		cm/mrad
503	x-xp	7.5200	2.6157	0.5501	0.055	0.000962
	y-yp	5.4201	2.3252	0.4874	0.019	0.000944

Table 3: Emittance and Twiss parameters of the beam at the trap

The transversal emittance is much bigger than that of the beam entering the solenoid, because the beam propagate only in the first half of the SC solenoid. Simulations were made to verify that the emittance come back to its initial value after propagating through the whole solenoid.

Super-conducting solenoid located behind the phase 2 LEBT

We use here the same device than the one used for phase 2, namely the RFQ2 type solenoid.

We will see that placing this normal conducting solenoid between the super-conducting one and the RFQ helps to further decrease the beam diameter in the trap. But it has several others advantages: reducing the RF noise in the trap by increasing the distance between the trap and the RFQ; preparing a space for differential pumping and for a beam position monitor.

However, as noticed before, increasing the distance between the output of the RFQ and the trap increase the length of the beam (see Fig. 6). We must look at the magnetic field induced by the SC solenoid in the shield of the RFQ2 type solenoid, and check whether it has an influence.

Combination of the fields of the two solenoid magnets

The magnetic fields were calculated with POISSON: Fig. 8 shows the magnetic field lines of the SC solenoid, with the RFQ2 type solenoid off.
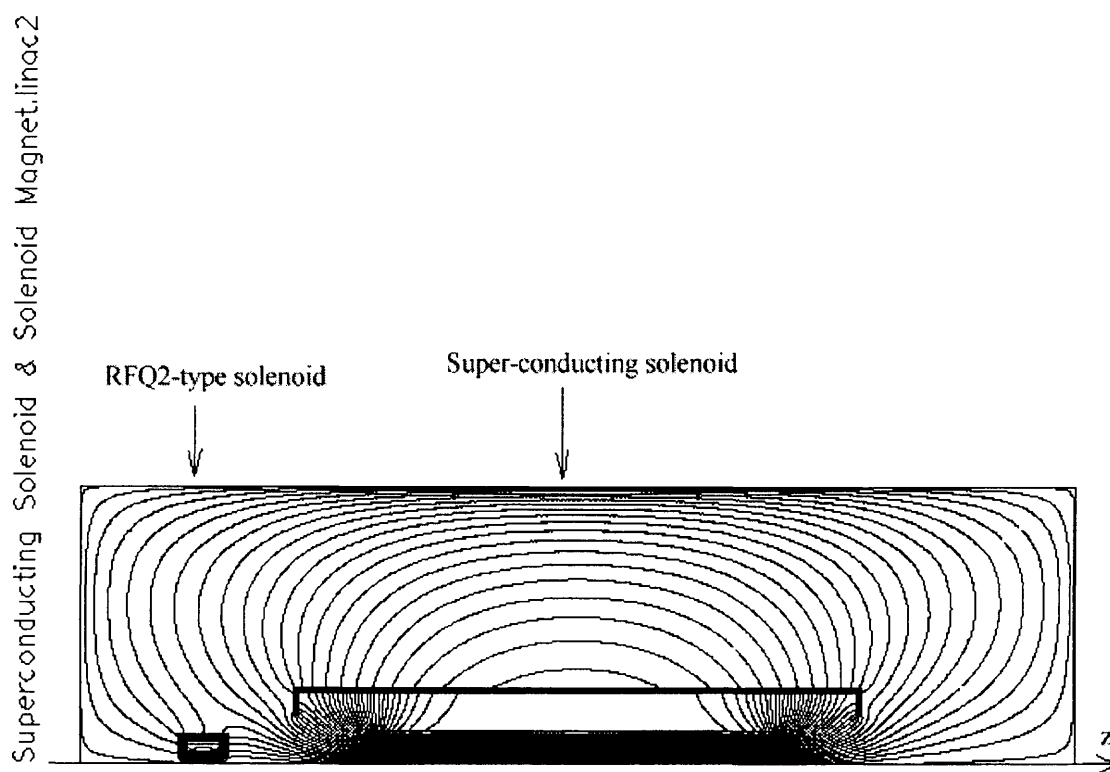

Fig. 8: Magnetic field lines of the SC solenoid, RFQ2 type solenoid is off.

To see whether the field of the RFQ2 type solenoid is perturbed, we have plotted (see Fig. 9 & 10) the longitudinal field B_z along the axis ($r=0$), for SC solenoid on (dotted lines) and off (continuous line). For the normal conducting solenoid, B_z is the same whether the SC solenoid is on or off.
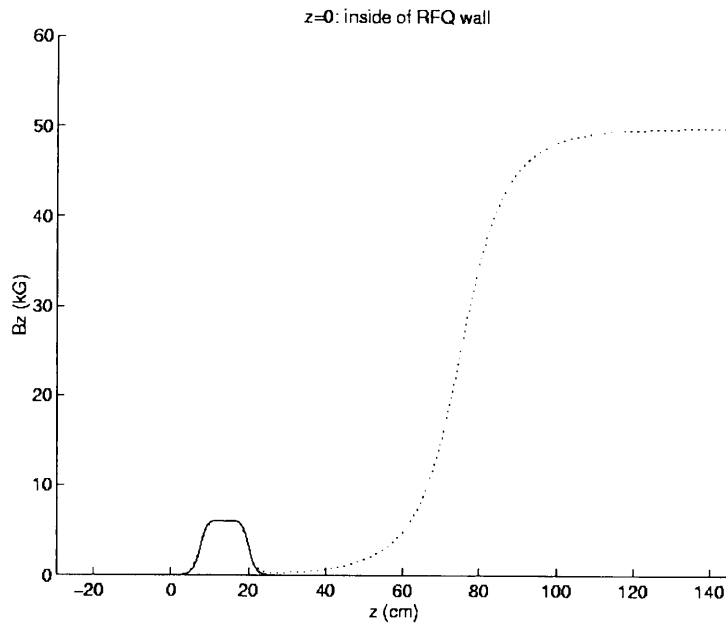
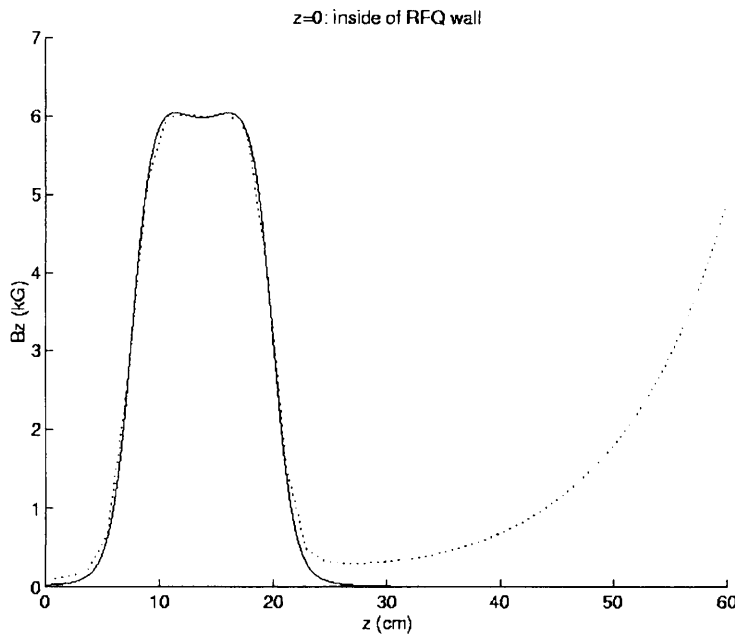z=0: inside of RFQ wall

Fig. 9

z=0: inside of RFQ wall

Fig. 10

Different trials to reduce the size of the beam in the trap

With the optimised set-up of the LEBT summarised on the scheme below, we achieved to reduce the size of the beam to 5 mm diameter (total size) at the trap center. There are 34% of the particles coming from the AD in a square delimited by [x=±1 mm, y=±1 mm]. The field strength of the normal conducting solenoid has been set to 6.12 kG to optimise the percentage of the particles that can be used in the trap.
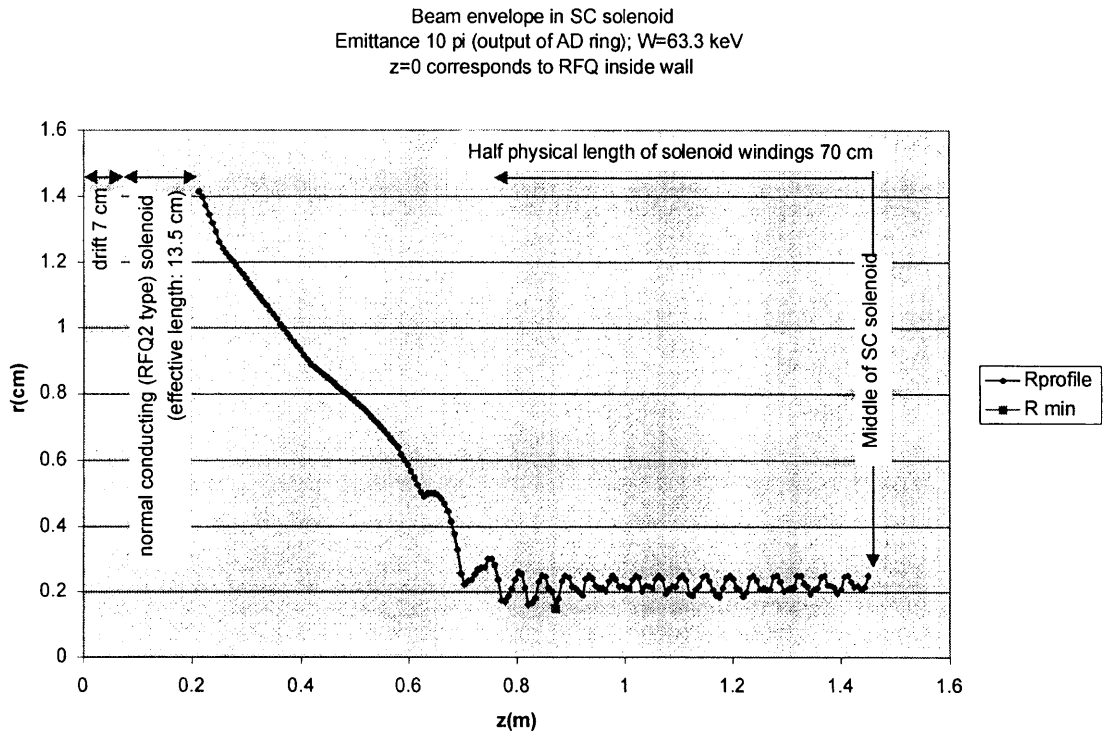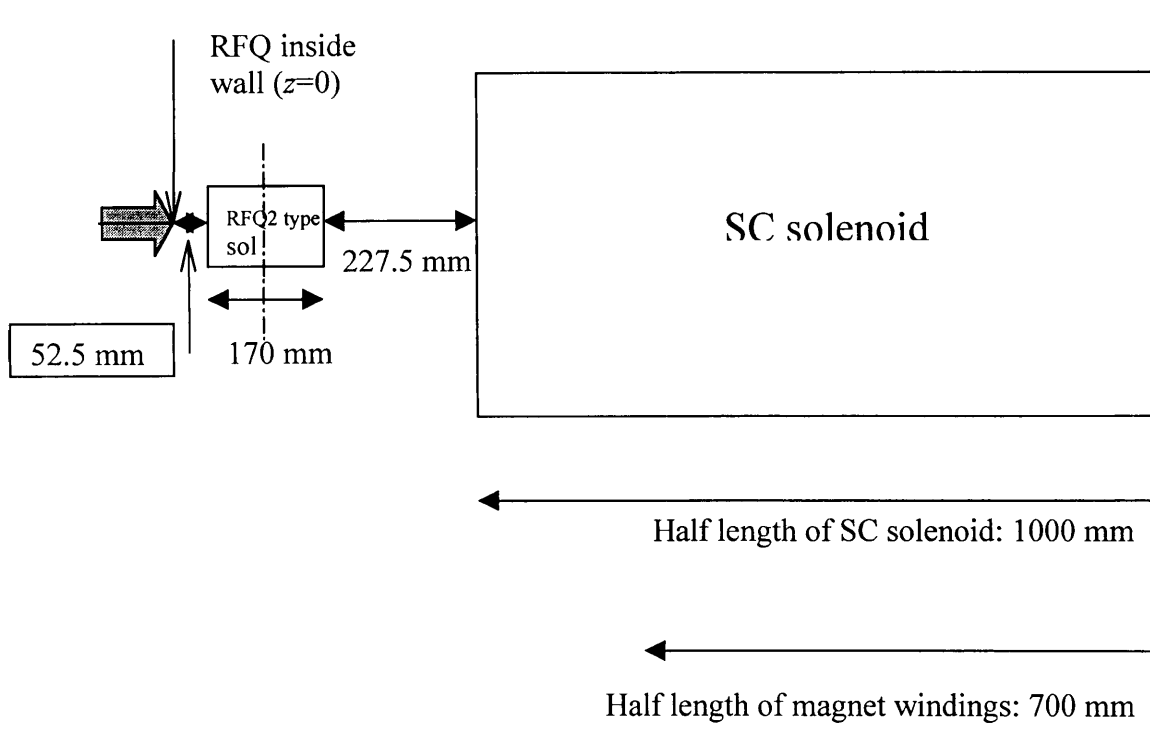
RFQ inside
wall (*z*=0)

RFQ2 type
sol

227.5 mm

52.5 mm

170 mm

SC solenoid

Half length of SC solenoid: 1000 mm

Half length of magnet windings: 700 mm

Beam envelope in SC solenoid
Emittance 10 pi (output of AD ring); W=63.3 keV
z=0 corresponds to RFQ inside wall

Half physical length of solenoid windings 70 cm

drift 7 cm

normal conducting (RFQ2 type) solenoid
(effective length: 13.5 cm)

Middle of SC solenoid

r(cm)

z(m)

Rprofile
R min

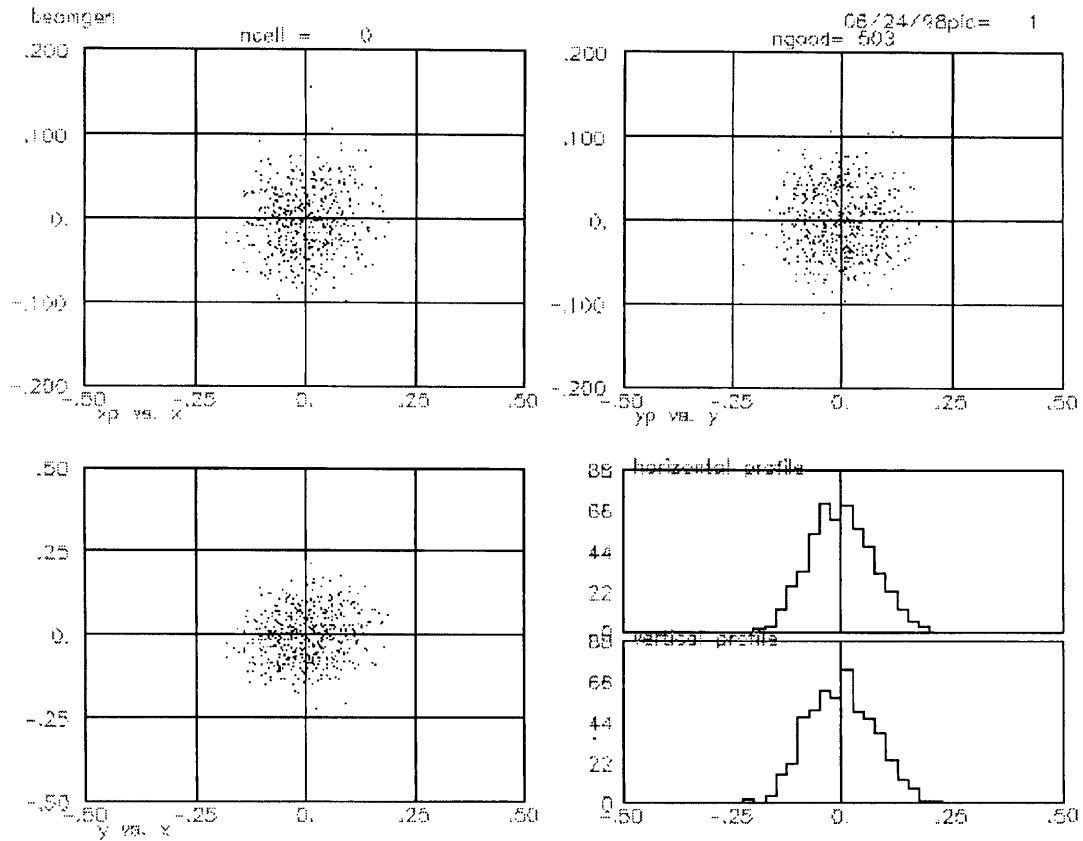Fig. 11: Beam envelope from the end of the RFQ2 type solenoid to the trap

Fig. 12: Beam at the trap center, z=1450mm (position in cm, divergence in rad)

Numb. of particles	Plane	Emittance,cm.mrad (normalised)			Alpha	beta(u)
		100%	90%	Rms(n)		cm/mrad
503	x-xp	0.4156	0.1337	0.0317	-0.103	0.001537
	y-yp	0.8777	0.1300	0.0323	-0.001	0.001615

Table 4: Twiss parameter of the beam at the trap center (z=1450mm)

Fig. 11 shows the envelope of the beam from the end of the normal conducting solenoid to the trap. Fig. 12 and Table 4 shows the beam and its Twiss parameters at the trap.

Looking at the beam envelope on Fig. 11, we see that the shape is not the same as that plotted on Fig. 7. Due to the action of the normal conducting solenoid, the beam is now converging at beginning of the SC solenoid. However, we tried to put the degrader foil where the beam diameter is minimum (namely z=870 mm as pointed out in Fig. 11) to see if the size of the beam could be reduce at z=1450 mm.

The degrader foil, is also necessary to help to the capture of the antiprotons in the trap, by reducing their energy to some 10 keV. The drawback of this solution is that it could lead to a loss of particles when passing through the foil, and to angular/energy straggling of the beam.

First we put the degrader foil at z=870 mm, reducing the energy to 10 keV. The simulations were performed with 10,000 particles coming out from the AD, in order to avoid effects of the statistic. Results are plotted on Fig. 13.
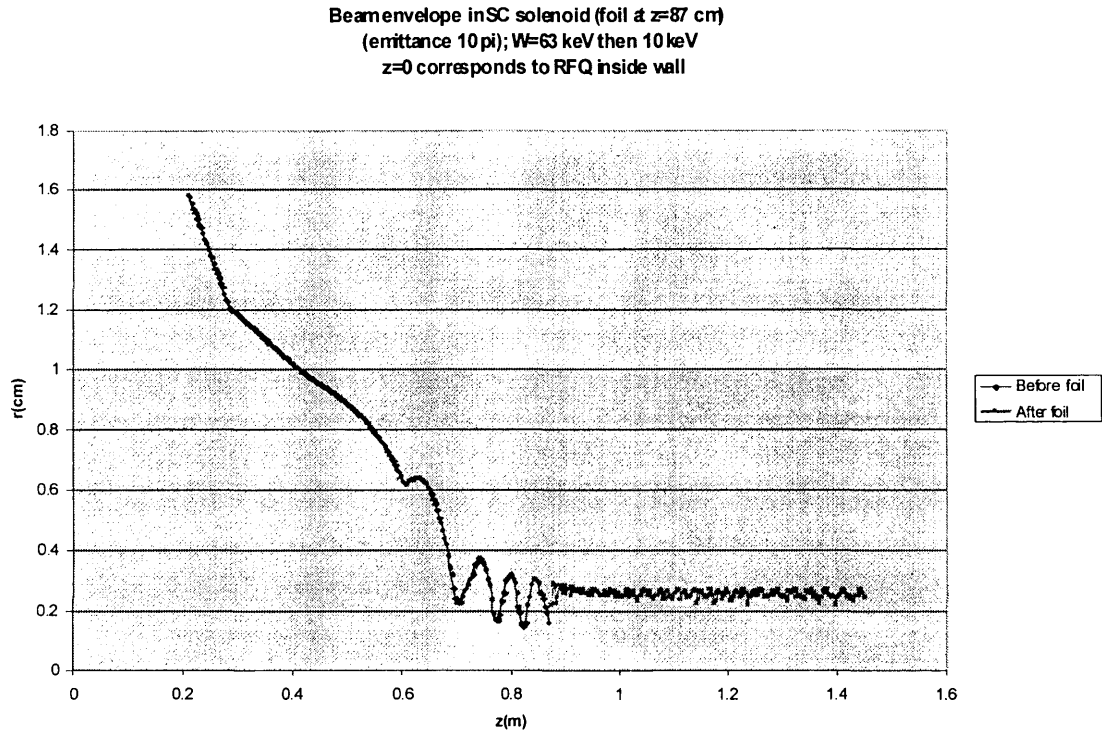
Beam envelope in SC solenoid (foil at z=87 cm)
(emittance 10 pi); W=63 keV then 10 keV
z=0 corresponds to RFQ inside wall

Fig. 13

The total diameter of the beam is still around 5 mm, but the percentage of "good" antiprotons (after filtering between 0 and 15 keV and ±1 mm transversally) is slightly improved: 36%.

Another trials has been achieved, with the degrader foil located at a position where the spot size is still large but the beam is still converging, and with a weaker degradation. Fig. 14 shows for instance a configuration with the foil at z=602 mm.
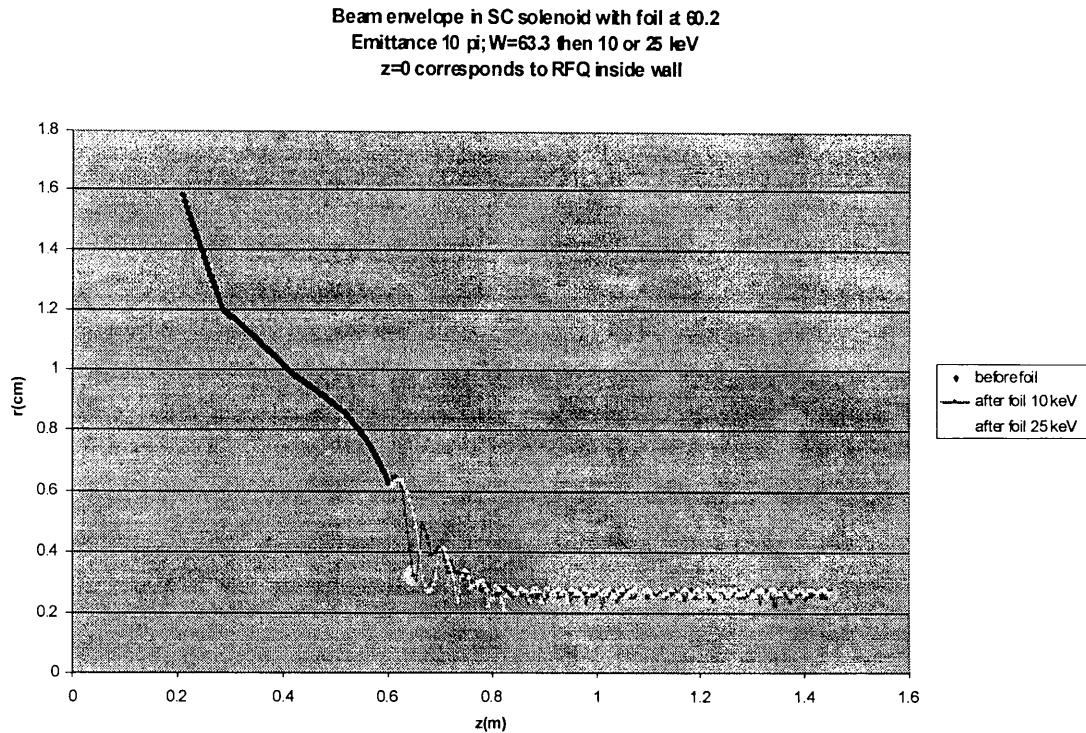
Beam envelope in SC solenoid with foil at 60.2
Emittance 10 pi; W=63.3 then 10 or 25 keV
z=0 corresponds to RFQ inside wall

Fig. 14

For the 10 keV beam after the foil, when filtering between 0 and 15 keV and ±1 mm transversally, the percentage of the antiprotons (coming from the AD) left is 37.5%.
For the 25 keV beam after the foil, when filtering between 20 and 30 keV and ±1 mm transversally, the percentage of the antiprotons (coming from the AD) left is 34.5%.

With all the different configurations tested, we hit the limit of ~5 mm beam diameter.

Conclusion

A set-up for a Low Energy Beam Transport line between AD-RFQ and ASACUSA experiments has been calculated and optimised.
For phase 2, this consists either of a triplet of quadrupoles, or a solenoid. The solution with the RFQ2-type solenoid is the simplest one, leading to a much smaller beam diameter of 4.9 mm at the formvar window. However, we must keep the first solution with the three quadrupoles in mind, in case of the beam coming out from the RFQ is not perfectly well symmetric.
For phase 3, the LEBT consists, as in phase 2 second solution, in the RFQ2 type solenoid. This leads to a beam diameter of roughly 5 mm in the trap, wherever the degrader foil is located. The different values of the energy tested downstream the foil doesn't seem to change anything in the size of the beam.